

# Axion Clouds around Neutron Stars

Dion Noordhuis,<sup>1,\*</sup> Anirudh Prabhu,<sup>2,†</sup> Christoph Weniger,<sup>1,‡</sup> and Samuel J. Witte<sup>1,3,§</sup>

<sup>1</sup>*GRAPPA Institute, Institute for Theoretical Physics Amsterdam and Delta Institute for Theoretical Physics, University of Amsterdam, Science Park 904, 1098 XH Amsterdam, The Netherlands*

<sup>2</sup>*Princeton Center for Theoretical Science, Princeton University, Princeton, NJ 08544, USA*

<sup>3</sup>*Departament de Física Quàntica i Astrofísica and Institut de Ciències del Cosmos (ICCUB), Universitat de Barcelona, Diagonal 647, E-08028 Barcelona, Spain*

Recent work has shown that axions can be efficiently produced via non-stationary pair plasma discharges in the polar cap region of pulsars. Here, we point out that for axion masses  $10^{-9} \text{ eV} \lesssim m_a \lesssim 10^{-4} \text{ eV}$ , a sizable fraction of the sourced axion population will be gravitationally confined to the neutron star. These axions accumulate over astrophysical timescales, thereby forming a dense ‘axion cloud’ around the star. We argue that the existence of such a cloud, with densities reaching and potentially exceeding  $\mathcal{O}(10^{22}) \text{ GeV cm}^{-3}$ , is a generic expectation across a wide range of parameter space. For axion masses  $m_a \gtrsim 10^{-7} \text{ eV}$ , energy is primarily radiated from the axion cloud via resonant axion-photon mixing, generating a number of distinctive signatures that include: a sharp line in the radio spectrum of each pulsar (located at the axion mass, and with a percent-level width), and transient events arising from the reconfiguration of charge densities in the magnetosphere. While a deeper understanding of the systematic uncertainties in these systems is required, our current estimates suggest that existing radio telescopes could improve sensitivity to the axion-photon coupling by more than an order of magnitude.

## I. INTRODUCTION

A generic prediction of several extensions of the Standard Model of particle physics is the existence of light pseudoscalars known as axions. Perhaps the best-known example is the ‘QCD axion’, a pseudo-Goldstone boson arising in the leading solution to the Strong-CP problem (this is the question of why charge-parity symmetry is preserved in quantum chromodynamics) [1–4]. Light axions are also a standard feature appearing from the compactification of extra dimensions in well-motivated extensions of the Standard Model (such as *e.g.* String Theory [5–9]), and are among the leading candidates to explain the ‘missing matter’ in the Universe, *i.e.* dark matter (see *e.g.* [10] for a recent review).

One of the novel and more compelling proposals to indirectly search for axions involves looking for radio signals coming from the magnetospheres of neutron stars. The large magnetic fields and ambient plasma found in these environments can dramatically enhance the interaction rate between axions and electromagnetism, producing an array of distinctive signatures. These include radio spectral lines arising from the resonant conversion of axion dark matter [11–23], broadband radio emission generated from axions sourced in the polar caps of pulsars [24, 25], and transient radio bursts [22, 26–34].

In this article, we show that the mere existence of an axion with a mass in the range  $10^{-9} \text{ eV} \lesssim m_a \lesssim 10^{-4} \text{ eV}$  leads to the generic prediction that all neutron stars are surrounded by extremely dense clouds of axions. This is

a direct consequence of the fact that iterative bursts of  $e^\pm$  pair production taking place in the polar caps of active neutron stars induce a quasi-periodic dynamical screening of  $\vec{E} \cdot \vec{B}$ , which enters as a source term in the axion’s equation of motion (here  $\vec{E}$  and  $\vec{B}$  are the electric- and magnetic field supported by the neutron star). Ref. [25] recently investigated the observable consequences arising from the high-energy part of the sourced axion population (*i.e.* the part which escapes the magnetosphere), showing that these axions can give rise to a substantial broadband radio flux. However, not all of the produced axions escape. For axion masses roughly in the MHz – GHz range, a large fraction of injected energy will go directly into axions that are instead gravitationally confined to the neutron star. Owing to their feeble interactions, these particles cannot efficiently dissipate energy, and will therefore accumulate on astrophysical timescales. Importantly, the enormous densities realized in these environments allow one to overcome the traditional challenges associated with detecting feebly interacting particles; as such, the existence of dense axion fields around neutron stars will not only have a profound impact on existing indirect axion searches (such as those in [20, 21, 23, 25]), but will also open a new regime of axion phenomenology that carries enormous discovery potential.

The goal of this paper is to explore the formation, the properties, and the evolution of axion clouds around neutron stars, setting the stage for future studies of the phenomenological implications of these systems. We achieve this by simulating the evolution of a small population of neutron stars from birth to death, tracing the change in the axion production rate due to magneto-rotational spin-down, and looking at the extent to which energy stored in the axion cloud can be dissipated over the course of a neutron star’s lifetime. We show that for typi-

\* [d.noordhuis@uva.nl](mailto:d.noordhuis@uva.nl)

† [prabhu@princeton.edu](mailto:prabhu@princeton.edu)

‡ [c.weniger@uva.nl](mailto:c.weniger@uva.nl)

§ [switte@icc.ub.edu](mailto:switte@icc.ub.edu)

cal neutron stars in our sample, the characteristic density of axions near the surface of the star can exceed the local dark matter density by more than twenty orders of magnitude (even for relatively small axion-photon couplings) over a sizable fraction of the neutron star lifetime. We also investigate how energy is dissipated in axion clouds, showing that resonant axion-photon conversion can generate a number of distinct and powerful observational signatures at radio frequencies.

This manuscript is organized as follows. We begin in Sec. II by discussing the fundamental physics governing the formation and evolution of axion clouds. This includes a thorough discussion of various mechanisms capable of dissipating the stored energy; here, we show that the dominant energy dissipation mechanism is typically resonant axion-photon mixing. One inevitable consequence that arises from this mixing is the production of radio emission – this is the focus of Sec. III. In this section we identify two unique signatures arising from the existence of axion clouds<sup>1</sup>: a sharp kinematic feature in the radio band appearing at the axion mass, and a transient radio burst which serves to dissipate the axion cloud late in a neutron star’s lifetime. We furthermore estimate projected sensitivities of existing radio telescopes to both signatures in Sec. IV. We provide concluding remarks in Sec. V.

## II. AXION CLOUDS

The first model for a plasma-filled magnetosphere was introduced more than fifty years ago, when Ref. [36] noted that the parallel component of the induced electric field,  $E_{\parallel} \equiv (\vec{E} \cdot \vec{B})/|\vec{B}| \neq 0$ , can easily overpower gravity, naturally leading to the extraction of charges directly from the upper layers of a neutron star’s surface. The extracted current drives electric fields which attempt to screen  $E_{\parallel}$ , eventually pushing the system toward a steady-state configuration in which  $E_{\parallel} = 0$  everywhere [36]. This solution, known as the Goldreich-Julian (GJ) model, requires the plasma to co-rotate with the neutron star, a feat which is impossible at sufficiently large radial distances.

As a result, small localized regions known as vacuum gaps, with  $E_{\parallel} \neq 0$ , are expected to appear in order to supplement the plasma deficit at large radii [37]. As mentioned above, however, the existence of a large  $E_{\parallel}$  component is unstable. The parallel electric field will extract and accelerate primary particles from the neutron star surface – these particles will subsequently ignite  $e^{\pm}$  pair

<sup>1</sup> A companion paper by a subset of the authors also illustrates how at low axion masses, below those studied here, the axion cloud can dissipate energy by driving radiative energy losses in the plasma itself. In this regime, the axion cloud can back-react on the electrodynamics in the polar cap, imprinting a periodic nulling on a pulsar’s radio emission [35].

cascades, generating a dense plasma which temporarily screens  $E_{\parallel}$  before flowing away from the neutron star. Recent years have shown significant progress in simulating this dynamical discharge process taking place in the polar cap gaps (*i.e.* the vacuum gaps situated just above the magnetic poles of a neutron star), indicating that it may be the source of the coherent radio emission observed from pulsars [38, 39].

It was recently demonstrated that the dynamical screening of  $E_{\parallel}$  in the polar caps can also efficiently source a local population of axions [24, 25] – this is a consequence of the fact that  $\vec{E} \cdot \vec{B}$  enters as a source term in the axion’s equation of motion. The spectrum of emitted axions is determined by the induced oscillations that arise from the screening process, and is expected to roughly span frequencies in the MHz – GHz range (consistent with the spectrum of observed radio emission). Relativistic axions produced in this way can escape the gravitational pull of the neutron star – during their traversal of the magnetosphere these axions can, on occasion, resonantly convert to low-energy radio photons. Ref. [25] used a combination of semi-analytic modeling, numerical simulations, and geometric ray-tracing to compute the spectra of escaping axions and photons sourced in the magnetospheres of nearby pulsars. By comparing the predicted and observed radio flux from this pulsar population, Ref. [25] was able to set stringent constraints on the axion-photon coupling across a wide range of axion masses.

In this manuscript, we focus instead on the implications arising from non-relativistic axions sourced in the polar caps, which can comprise a sizable fraction of the total axion population if the axion mass is roughly in the range  $10^{-9} \text{ eV} \lesssim m_a \lesssim 10^{-4} \text{ eV}$ . These non-relativistic axions are gravitationally bound to the neutron star, and will therefore accumulate over time, resulting in the formation of a dense axion cloud<sup>2</sup>. In this section we study the evolution of these clouds over the lifetime of the neutron star, showing that an axion cloud proceeds through four distinct phases – these phases are highlighted in Fig. 1.

### A. General evolution

Axions generically couple to electromagnetism via the Lagrangian term  $\mathcal{L} \supset -\frac{1}{4}g_{a\gamma\gamma} a F_{\mu\nu} \tilde{F}^{\mu\nu}$ , where  $F$  and  $\tilde{F}$

<sup>2</sup> Basins of light bosonic particles around stellar objects have been studied in *e.g.* [40, 41]. These studies are qualitatively similar to the analysis presented here, but rely on volumetric thermal emission in the Sun. In contrast, we study non-thermal emission arising from pulsar polar caps; the case of thermal emission from neutron stars is not expected to produce large densities as it necessitates much larger axion masses in order to be effective, and these axions are efficiently absorbed inside of the neutron star.

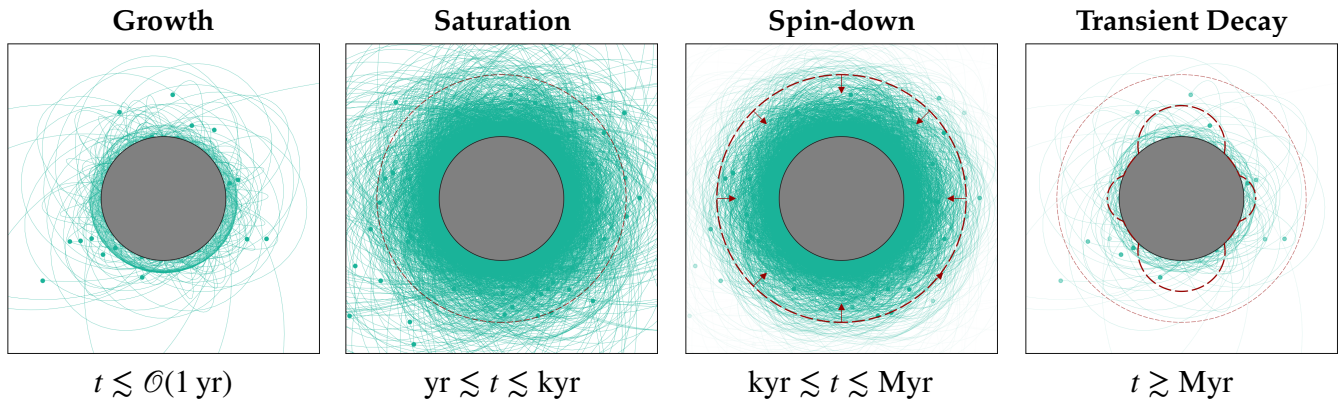


FIG. 1. Overview of the four stages characterizing the formation and evolution of axion clouds around neutron stars. **Growth** (left): typically occurring on sub-year timescales, the axion cloud grows in an unimpeded manner. **Saturation** (center-left): occurring on  $\mathcal{O}(\text{yr})$  to  $\mathcal{O}(\text{kyr})$  timescales, the outer part of the density profile saturates as a result of resonant axion-photon conversion (taking place near the conversion surface shown as a dashed red line). The inner part of the profile is unaffected by the resonant transitions, and continues to grow. **Spin-down** (center-right): occurring on  $\mathcal{O}(\text{kyr})$  to  $\mathcal{O}(\text{Myr})$  timescales, the neutron star undergoes magneto-rotational spin-down, causing the production rate of axions to decrease and shifting the resonant conversion surface to smaller radii. **Transient Decay** (right): late in the neutron star's lifetime axion production ceases and the magnetosphere relaxes to a fully charge-separated state. This process opens resonant transitions at all radii, and causes the axion cloud to fully dissipate its energy.

are the electromagnetic field strength tensor and its dual,  $a$  is the axion field, and  $g_{a\gamma\gamma}$  is the coupling strength. The resulting axion equation of motion is given by

$$(\square + m_a^2) a(x) = -g_{a\gamma\gamma} (\vec{E} \cdot \vec{B})(x), \quad (1)$$

where  $\vec{E} \cdot \vec{B}$  clearly appears as an axion source term. Following Ref. [25], one can express the differential production rate of axions from spacetime variations in the source term via

$$\frac{d\dot{N}_a}{d^3k} = \frac{|\tilde{\mathcal{S}}(\vec{k})|^2}{2(2\pi)^3 \omega_a(\vec{k}) T}. \quad (2)$$

Here  $\omega_a(\vec{k})$  is the energy of mode  $\vec{k}$ ,  $T$  is the characteristic period of the gap discharge process, and  $\tilde{\mathcal{S}}(\vec{k})$  is the Fourier transform (FT) of the source term, *i.e.*

$$\tilde{\mathcal{S}}(\vec{k}) = -g_{a\gamma\gamma} \int d^4x e^{ik \cdot x} (\vec{E} \cdot \vec{B})(x). \quad (3)$$

From Eq. 3, one can see that the production rate and spectrum of axions produced during the screening of the vacuum gap is fully resolved by the spacetime evolution of  $E_{\parallel}$ , which is non-trivial due to pair production processes.

In order to make general statements about the properties of axion clouds, we simulate the evolution of ten different neutron stars over the course of their lifetime. Following Refs. [42, 43], we assume the initial period ( $P$  in seconds), magnetic field ( $B_0$  in Gauss), and misalignment angle ( $\chi$  in degrees) are uncorrelated at birth, and

characterized by the following distributions

$$p(P) = \frac{1}{\sqrt{2\pi\sigma_p^2}} e^{-(P-\mu_p)^2/(2\sigma_p^2)}, \quad (4)$$

$$p(B_0) = \frac{1}{\sqrt{2\pi\sigma_B^2}} e^{-(\log_{10}(B_0)-\mu_B)^2/(2\sigma_B^2)}, \quad (5)$$

$$p(\chi) = \sin \chi/2. \quad (6)$$

Here, the means and standard deviations have been obtained by performing fits to the observed pulsar population, and are given by  $\mu_p = 0.22$ ,  $\sigma_p = 0.42^3$ ,  $\mu_B = 13.2$ , and  $\sigma_B = 0.62$ . The initial conditions for the ten neutron stars in our sample are obtained via random draws from Eqs. 4–6; the properties of each neutron star at birth are presented in the first columns of Table I.

For active neutron stars, the rate of spin-down is determined by a combination of dipole radiation and plasma effects (see *e.g.* [44, 45]). The evolution of the rotational period and alignment angle are given by

$$\dot{P} = \beta \frac{B_0^2}{P} (\kappa_0 + \kappa_1 \sin^2 \chi), \quad (7)$$

$$\dot{\chi} = -\beta \kappa_2 \frac{B_0^2}{P^2} \sin \chi \cos \chi, \quad (8)$$

where  $\kappa_0 \sim \kappa_1 \sim \kappa_2 \sim 1$  and  $\beta = \pi^2 R_{\text{NS}}^6 / I_{\text{NS}} \sim 6 \times$

<sup>3</sup> Note that the distribution of the period is restricted to the positive definite domain, and the misalignment angle  $\chi$  is restricted to be between 0 and 90 degrees (pulsar evolution proceeds identically regardless of whether the projection of the magnetic axis onto the rotational axis is positive or negative).

| NS | $P_{\text{Birth}}$ (s) | $B_{0,\text{Birth}}$ (G) | $\chi_{\text{Birth}}$ (deg) | $P_{\text{Death}}$ (s) | $B_{0,\text{Death}}$ (G) | $\chi_{\text{Death}}$ (deg) |
|----|------------------------|--------------------------|-----------------------------|------------------------|--------------------------|-----------------------------|
| 1  | 0.186                  | 2.88E13                  | 48                          | 3.40                   | 3.94E12                  | 5                           |
| 2  | 0.168                  | 1.39E14                  | 23                          | 10.8                   | 3.99E13                  | 0.41                        |
| 3  | 0.094                  | 1.73E13                  | 46                          | 2.16                   | 1.59E12                  | 3.7                         |
| 4  | 0.429                  | 2.24E12                  | 62                          | 0.587                  | 1.17E11                  | 58                          |
| 5  | 0.158                  | 3.76E13                  | 9.7                         | 4.18                   | 5.95E12                  | 0.37                        |
| 6  | 0.533                  | 5.89E12                  | 80                          | 1.21                   | 4.97E11                  | 75                          |
| 7  | 0.486                  | 1.49E13                  | 74                          | 2.51                   | 2.14E12                  | 55                          |
| 8  | 0.990                  | 2.00E13                  | 14                          | 2.65                   | 2.38E12                  | 5.5                         |
| 9  | 0.700                  | 1.04E12                  | 51                          | 0.722                  | 1.78E11                  | 50                          |
| 10 | 0.054                  | 1.00E13                  | 86                          | 1.76                   | 1.06E12                  | 65                          |

TABLE I. Listed properties of the mock neutron stars used in this work. The columns denote: neutron star number, period at birth (in seconds), surface magnetic field strength at birth (in Gauss), misalignment angle at birth (in degrees), period at death (in seconds), surface magnetic field strength at death (in Gauss), and misalignment angle at death (in degrees).

$10^{-40} \text{ G}^{-2} \text{ s}$ , with  $R_{\text{NS}}$  and  $I_{\text{NS}}$  being the neutron star radius and moment of inertia respectively.

Detailed modeling of magnetic field evolution in neutron stars is an active area of research that involves detailed simulations of internal neutron star conductivity (see [46–48] for recent progress). The main processes governing the evolution of neutron star magnetic fields are: Ohmic dissipation, Hall drift, and ambipolar diffusion. Ohmic dissipation simply describes the energy losses that arise from having a finite conductivity internal to the neutron star. The rate of Ohmic dissipation can be enhanced by Hall drift, which allows for magnetic flux to be transported from inner regions of the star, where the rate of energy dissipation is slow, to the outer crust, where the rate is considerably higher. Ambipolar diffusion arises due to relative motion between charged particles and neutrons, leading to a drag that dissipates energy – this dissipation mechanism is typically only efficient early in the lifetime of neutron stars with extremely large magnetic fields. Here, we make the simplifying assumption that magnetic field evolution is dominated by Ohmic dissipation, which drives exponential decay of the magnetic field on a timescale  $\tau_{\text{ohm}}$ , *i.e.*

$$\dot{B}_0 = -B_0/\tau_{\text{ohm}}. \quad (9)$$

We take  $\tau_{\text{ohm}}$  to be 1 Myr [43, 49], which is expected to lie on the very conservative<sup>4</sup> end of the spectrum as the simulations of [43, 49] assume that the currents supporting the magnetic field are confined to the crust – should the currents also penetrate the core, as may be expected, the Ohmic decay timescale could increase by orders of magnitude. Our treatment neglects the impact of Hall drift and ambipolar diffusion, which can induce small corrections to high-magnetic field neutron stars on shorter

timescales. Properly including such contributions, however, requires more refined modeling and a better understanding of the behaviour of currents in the stellar interior.

The properties of the ten neutron stars considered in this work, at both birth and death, are displayed in Table I<sup>5</sup>. We define the point of death as the time at which the neutron star is no longer able to produce radio emission – this occurs when the rotational period falls below  $P \simeq 1.7 \text{ s} \sqrt{B_0/10^{12} \text{ G}}$  [50]. Once a neutron star crosses this point we also assume that it is no longer able to generate axions. For each neutron star in our sample, we utilize the semi-analytic model of [25] to predict the axion spectrum at birth, 10 yrs, 100 yrs, 1 kyr, 10 kys, 100 kys, and at death. These spectra allow for the smooth interpolation of the production rate of axions throughout the lifetime of the neutron star.

The time evolution of the axion spectra can subsequently be used to reconstruct the density profile of axions around the neutron stars at any given time. In order to achieve this we first note that Eq. 2 describes the number of axions produced with a given  $k$ -mode across the entirety of the gap – if the gap is sufficiently small (such that the gradient of the gravitational potential across the gap can be neglected), one can assume all axions in a narrow range of  $k$ -modes follow approximately the same trajectory. Adopting this approximation, we take  $\sim 10^4$  logarithmically spaced bins over momenta  $k < k_{\text{esc}}$  (where  $k_{\text{esc}}$  is the escape momentum), and trace the evolution of these bound trajectories over timescales on the order of  $\tau_0 \sim \mathcal{O}(1 - 10^3)$  seconds (corresponding to  $10^3 - 10^4$  neutron star crossing times). Considering all trajectories,

<sup>4</sup> Note that small Ohmic decay times are ‘conservative’ in that, under the assumption of a fixed neutron star formation rate, they suppress the size of the active pulsar population.

<sup>5</sup> Notice that the magnetic field of one of our neutron stars exceeds the Schwinger field strength  $B_Q \simeq 4.4 \times 10^{13} \text{ G}$ . In this limit, the gap dynamics and charge configuration may deviate from that of standard pulsars. In what follows, we treat this neutron star with the same dynamics as the others, but we avoid making any statements that rely on the properties of this outlier.

we identify the points at which they cross a given shell of radius  $r$ , and average the energy density of axions contained in the trajectories over this shell – this procedure yields a radial density profile at  $\tau_0$  given by

$$\begin{aligned} \rho(r, \tau_0) &= \frac{1}{A} \int dA n_a(r) \omega_a(r) \\ &\sim \frac{1}{4\pi r^2} \sum_{k_j, x} \frac{\omega_{j,x} \dot{N}_{j,x}}{v_{j,x} \cos \theta_{j,x}}. \end{aligned} \quad (10)$$

Here we have used the fact that one can express the number density  $n_a$  in terms of the axion production rate  $\dot{N}_a$ , *i.e.*  $n_a \equiv dN_a/d^3x = dN_a/(v_a \cos \theta dA dt)$  (where  $dA$  is the area element with a surface normal oriented at an angle  $\theta$  with respect to the axion velocity  $v_a$ ). The summation runs over the trajectories  $k_j$  and the crossings  $x$  of each trajectory with the radial surface located at  $r$ .

In the event that axions can be treated as fully non-interacting, the density profile is expected to grow linearly as long as the properties of the neutron star remain constant (*i.e.* on timescales shorter than the spin-down and magnetic field decay timescales). This is conservatively expected to last on the order of  $\tau_{\text{linear}} \sim \mathcal{O}(\text{kyr})$ . On longer timescales, magneto-rotational spin-down decreases axion production, leading to an eventual saturation of the growth. We incorporate the effect of spin-down into the evolution of the density profile at a given time  $\tau$  by re-scaling Eq. 10 by a factor of  $\tau/\tau_0$ , and redefining  $\dot{N}_{j,x}$  with an effective production rate  $\dot{N}_{j,x}^{\text{eff}}$ , which is obtained at each  $\tau$  by interpolating between the axion production rates of the trajectories as computed over the lifetime of the neutron star. As we discuss below, there moreover exist various mechanisms which can dissipate energy or disrupt the production of axions. As a result, for large axion couplings the assumption of linear growth on short timescales may not hold, and the growth of the cloud may be saturated long before spin-down substantially abates axion production.

## B. Energy dissipation mechanisms

In order to properly follow the long-term evolution of the axion cloud, one must understand the extent to which the feeble interactions of the axion can dissipate energy, or back-react on the production process itself. Here, we investigate a number of mechanisms which in this way could alter the linear growth of the axion density. These include: absorption by nuclei internal to the neutron star, axion self-interactions, and electromagnetic interactions. Our calculations suggest that the dominant mechanisms are typically expected to be electromagnetic.

### 1. Absorption

Axions have a dimension-5 coupling to nucleons via the Lagrangian term

$$\mathcal{L} \supset \frac{1}{2} g_{aN} \partial_\mu \bar{N} \gamma^\mu \gamma_5 N, \quad (11)$$

which can induce inverse bremsstrahlung absorption (or bremsstrahlung emission) of axions as they traverse the nuclear matter interior to the neutron star<sup>6</sup>. Here, we show that for typical axion-nucleon couplings  $g_{aN}$  this absorption process is not expected to significantly impede the evolution of the cloud.

We start by noting that the evolution of a single axion trajectory with phase space  $f_a$  can be described by the one-dimensional Boltzmann equation (in flat space)

$$(\partial_t + v_a \partial_x) f_a = \Gamma_E (1 + f_a) - \Gamma_A f_a = \Gamma_E - \Gamma_{A*} f_a, \quad (12)$$

where  $\Gamma_E$  and  $\Gamma_A$  are the emission and absorption rate in vacuum, respectively. In the final expression we have defined the effective absorption rate  $\Gamma_{A*} \equiv \Gamma_A - \Gamma_E$ , which accounts for the fact that a high occupation number axion background can also stimulate the bremsstrahlung emission of new axions. If the nuclear matter is in local thermal equilibrium, detailed balance implies that locally  $\Gamma_E = e^{-\omega_a/T_{\text{NS}}} \Gamma_A$ , with  $\omega_a$  being the axion energy and  $T_{\text{NS}}$  being the neutron star temperature (see *e.g.* [54]). Since  $\omega_a \ll T_{\text{NS}}$  for all axions in the cloud, it follows that  $\Gamma_{A*} \approx (\omega_a/T_{\text{NS}}) \Gamma_A \ll \Gamma_A$ , and thus the absorption rate tends to be heavily suppressed in these systems.

In order to provide a quantitative estimate of the absorption timescale, we use the Fermi surface approximation to compute the axion-nucleon bremsstrahlung mean free path. Details can for example be found in [55, 56]. Assuming the mean free path is constant through the neutron star, the fraction of axions absorbed via a single pass is given by

$$f_{\text{abs}} = \frac{N_{\text{ab}}}{N_0} = \left(1 - e^{-x/l_a^{\text{eff}}}\right), \quad (13)$$

where  $x$  is the distance travelled inside of the star and  $l_a^{\text{eff}} = l_a/(\omega_a/T_{\text{NS}})$  is the effective mean free path (including the factor due to stimulated emission). By tracing axion trajectories over many crossings and applying Eq. 13 to each, we can determine the typical timescale on which axion absorption takes place – we define this timescale to be  $\tau_{90}$ , which is the time after production when 90% of the axions on a given trajectory will have been absorbed.

In computing the absorption cross section we adopt a characteristic value for the internal temperature of  $T_{\text{NS}} = 10^6$  K and the nucleon Fermi momenta of  $p_{F_N} \sim$

<sup>6</sup> Other absorption channels are also possible, but always subdominant to axion-nucleon bremsstrahlung [51–53].

300 MeV. Furthermore using an axion-nucleon coupling of  $g_{aN} = 10^{-10} \text{ GeV}^{-1}$ , we find that low-energy axions (whose maximal radial distance from the neutron star is  $r_{\text{max}} \leq 20 \text{ km}$ ) have  $\tau_{90} \sim 100 \text{ yrs} - 1 \text{ kyr}$ . We determined empirically that this timescale grows roughly  $\propto r_{\text{max}}^{1.4}$  for axions produced with larger initial energies. In the next section, we show that unless there exists a large hierarchy between the axion-photon and axion-nucleon coupling,  $g_{a\gamma\gamma}/g_{aN} \ll 10^{-2}$ , absorption is unlikely to quench the growth of the axion cloud. The axion-nucleon coupling is thus not expected to have a sizable impact in most axion models, and we therefore set  $g_{aN} = 0$  in the rest of this manuscript.

### 2. Self-interactions

Non-linear corrections from the axion potential can lead to an alteration of the axion production rate. Taking the canonical instanton potential,  $V(a) \propto (1 - \cos(a/F_a))$ , as a representative example, one can see that self-interactions become important if  $a/F_a \sim \mathcal{O}(1)$ . Here  $F_a$  is the axion decay constant. In order to remain in the linear regime, we are thus constrained to densities  $\rho_L \lesssim m_a^2 F_a^2$ . Approximating  $g_{a\gamma\gamma} \sim F_a^{-1}$ , one can then estimate the typical density at which non-linearities become important. For an axion of mass  $m_a = 10^{-6} \text{ eV}$  and an axion-photon coupling of  $g_{a\gamma\gamma} = 10^{-11} \text{ GeV}^{-1}$ , this density is around  $\rho_{\text{NL}} \sim 10^{33} \text{ GeV cm}^{-3}$ . This is much larger than the typical densities reached in axion clouds (see next subsection); moreover, since the efficiency of axion production scales proportionally to  $g_{a\gamma\gamma}^2$  and  $\rho_{\text{NL}}$  scales with  $g_{a\gamma\gamma}^{-2}$ , we do not expect non-linear densities to be reached at any mass or coupling.

Self-interactions can further serve to quench the growth of the axion cloud via the  $3a \rightarrow a$  process. Here the final state axion has an energy  $\omega_a \sim 3 \times m_a$ , which is above the escape velocity of the neutron star. The rate of energy loss is given by [57]

$$\frac{dE_{3a \rightarrow a}}{dt} = 8\pi\omega_a^2 |\tilde{G}|^2, \quad (14)$$

where

$$\tilde{G} = \frac{1}{24\pi} \frac{m_a^2}{F_a^2} \int d^3x e^{-ik \cdot x} a(x)^3. \quad (15)$$

By equating the energy loss with the energy injection (here, we use the approximate expression for the energy injection derived in [35] in order to maintain the functional dependency on all quantities), we can determine the density and coupling at which axion emission could become important; this occurs at

$$\rho_{3a \rightarrow a} \sim 10^{26} \frac{\text{GeV}}{\text{cm}^3} \left( \frac{m_a}{10^{-6} \text{ eV}} \right)^{5/3} \left( \frac{10^{-12} \text{ GeV}^{-1}}{g_{a\gamma\gamma}} \right)^{2/3} \times \left( \frac{B_0}{10^{12} \text{ G}} \right)^{4/3} \left( \frac{\Omega_{\text{NS}}}{1 \text{ Hz}} \right)^{2/3}, \quad (16)$$

where for simplicity we have adopted characteristic values of the vacuum gap height and radius of  $h_{\text{gap}} \sim 10 \text{ m}$  and  $r_{\text{pc}} \sim 100 \text{ m}$  (see *e.g.* [25, 35] for the full expressions of these quantities). As we show below, this density is never realizable, and thus  $3a \rightarrow a$  axion emission cannot alter the growth of the axion cloud.

### 3. Electromagnetic interactions

Let us now turn our attention toward the impact of the electromagnetic coupling on the growth of the axion cloud. In general, this coupling can either (i) cause axions to drive oscillatory electromagnetic fields, which dissipate energy into the local plasma, or (ii) directly radiate low-energy photons. We discuss each of these possibilities below.

Ref. [35] recently investigated various mechanisms that can dissipate energy near a neutron star's surface. Owing to the strong in-medium suppression that arises around most neutron stars, Ref. [35] found that near the neutron star, energy dissipation occurs primarily in the vacuum phase of the polar cap gap discharge. At low masses ( $m_a \ll 10^{-7} \text{ eV}$ ), the axion induces an approximately homogeneous electric field that can cause the local current to emit additional curvature radiation, while at higher masses this effect washes out due to the rapid oscillations of the electric field. Instead, in the high axion mass regime the axion-induced electromagnetic fields can directly radiate on-shell photons. The maximal axion density at the neutron star surface that is achievable before these dissipation effects become relevant is roughly given by [35]

$$\rho_{\text{sat}} \sim 7 \times 10^{22} \frac{\text{GeV}}{\text{cm}^3} \left( \frac{m_a}{10^{-6} \text{ eV}} \right)^3 \left[ \frac{B_0}{10^{12} \text{ G}} \frac{\Omega_{\text{NS}}}{1 \text{ Hz}} \right]^{9/7} \mathcal{F} \quad (17)$$

for  $\lambda_a \geq h_{\text{gap}}$ , and

$$\rho_{\text{sat}} \sim 2 \times 10^{18} \frac{\text{GeV}}{\text{cm}^3} \left( \frac{m_a}{10^{-6} \text{ eV}} \right)^3 \times \left( \frac{B_0}{10^{12} \text{ G}} \right)^{18/7} \left( \frac{\Omega_{\text{NS}}}{1 \text{ Hz}} \right)^{39/7} \quad (18)$$

for  $\lambda_a < h_{\text{gap}}$ . Here  $\lambda_a$  is the de Broglie wavelength of the axion,  $\Omega_{\text{NS}}$  is the neutron star rotational velocity, and we have defined

$$\mathcal{F} = \begin{cases} 1 & \lambda_a \leq r_{\text{pc}} \\ (\lambda_a/r_{\text{pc}})^2 & \lambda_a > r_{\text{pc}} \end{cases}, \quad (19)$$

where  $r_{\text{pc}}$  is the polar cap radius [24, 25].

Eqs. 17 and 18 are derived under the assumption that the axion induced electric field remains small relative to the electric field of the neutron star itself; a careful analysis of the axion-modified Maxwell's equations suggests that this condition is violated when the axion density

near the neutron star reaches a value of [35]<sup>7</sup>

$$\rho_{\text{br}} \sim 10^{16} \frac{\text{GeV}}{\text{cm}^3} \left( \frac{\Omega_{\text{NS}}}{1 \text{ Hz}} \right)^2 \left( \frac{10^{-12} \text{ GeV}^{-1}}{g_{a\gamma\gamma}} \right)^2 \times \begin{cases} 1 & \lambda_a \geq h_{\text{gap}} \\ (k_a \times h_{\text{gap}})^2 & \lambda_a < h_{\text{gap}} \end{cases}. \quad (20)$$

At higher densities the back-reaction of the axion field becomes highly non-linear, and numerical simulations are likely required in order to understand whether the axion cloud can continue to grow. In order to remain conservative, in what follows we halt the growth of the cloud entirely when the axion density at the neutron star surface hits  $\rho_{\text{max}} \equiv \text{Min}[\rho_{\text{br}}, \rho_{\text{sat}}]$ . Note that as the neutron star evolves we continue to enforce  $\rho_a \leq \rho_{\text{max}}(B_0, \Omega_{\text{NS}})$ . For the masses studied here, we find that  $\rho_{\text{max}}$  is almost always determined by the back-reaction density.

A second prominent mechanism for electromagnetic energy dissipation in axion clouds is resonantly enhanced axion-photon mixing. This can occur when the local plasma frequency becomes comparable to the axion mass, *i.e.*  $\omega_p \simeq m_a$ . Here  $\omega_p = \sqrt{4\pi\alpha n_e/m_e}$ , with  $\alpha$  being the fine-structure constant,  $n_e$  the electron/positron number density, and  $m_e$  the electron mass. Whether or not such a condition is actually met over the course of an axion trajectory depends crucially on both the properties of the magnetosphere and on the energy of the axion. Extremely low-energy axions are effectively confined to radii  $r \lesssim R_{\text{NS}} + h_{\text{gap}}$ , and for most neutron stars the plasma density is likely to be large enough to kinematically block the resonance in these regions<sup>8</sup>. Axions with velocities near the escape velocity, however, will have large apoapses, implying they always traverse from regions with  $\omega_p \gg m_a$  to regions with  $\omega_p \ll m_a$ . Therefore, for these axions energy dissipation via resonant conversion is expected to be unavoidable. The net result is qualitatively different behaviour for the growth of the axion cloud at small and large radii.

In order to provide an illustrative example of the impact of resonant axion-photon mixing on the evolution of the axion cloud, we adopt a spherically symmetric plasma distribution normalized to the GJ plasma frequency at the pole (*i.e.* the  $e^\pm$  number density at the pole is set to  $n_e \equiv 2\vec{B}_0 \cdot \vec{\Omega}_{\text{NS}}/e$ ) [36], and with radial dependence

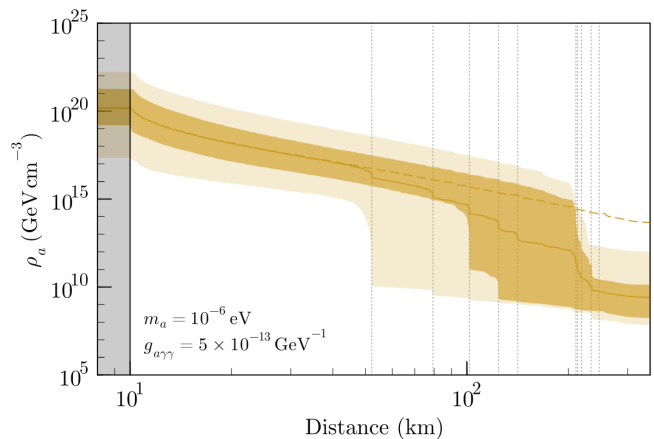


FIG. 2. Axion cloud density profile distribution after 1 kyr, and including continuous resonant transitions from a spherical conversion surface as defined in Eq. (21). The distribution mean is plotted along with its interquartile range (dark shaded area), minimum, and maximum (light shaded area). The constant neutron star radius is shown as a solid vertical line, with the area inside of the neutron star being greyed out. The density profile mean without resonant conversions is furthermore included as a dashed line, and the conversion radii of all considered neutron stars are shown as dotted vertical lines.

scaling like  $(r/R_{\text{NS}})^{-3/2}$ . Using this charge distribution, one can determine that resonant axion-photon transitions occur at a fixed radius  $r_c$  given by

$$r_c = 25 \text{ km} \left( \frac{R_{\text{NS}}}{10 \text{ km}} \right) \left[ \frac{B_0}{10^{12} \text{ G}} \frac{\Omega_{\text{NS}}}{1 \text{ Hz}} \left( \frac{10^{-6} \text{ eV}}{m_a} \right)^2 \right]^{1/3}. \quad (21)$$

The efficiency of conversions is expected to be roughly [15, 16, 18, 19]

$$P_{a \rightarrow \gamma} \simeq 1 - \exp \left[ -\frac{\pi}{2} \frac{g_{a\gamma\gamma}^2 B_c^2}{v_c |\omega'_p|} \right], \quad (22)$$

where  $v_c$  and  $B_c$  are the axion velocity and magnetic field at the conversion radius, and  $\omega'_p$  is the gradient of the plasma frequency projected onto  $\hat{v}_c$ . For simplicity, we have assumed in Eq. 22 that the magnetic field is always perpendicular to the axion velocity at conversion. The angular factors correcting for non-perpendicular propagation are not necessary for the rough estimates performed here, since the photon flux quickly becomes independent of conversion probability (this occurs due to the growth of the axion cloud reaching a state of equilibrium – see next paragraphs for more details).

Notice that, unlike previous studies in this field, we have chosen not to use the charge-separated GJ model; this model contains regions of pure vacuum extending to the surface of the neutron star (occurring when  $\vec{B}_0 \cdot \vec{\Omega}_{\text{NS}} = 0$ ), a feature which is likely not physical for young pulsars and which would dramatically enhance radio emission (the choice to remove these features thus leads to

<sup>7</sup> Note that the definition of the back-reaction density in the limit  $\lambda_a < h_{\text{gap}}$  differs slightly from the quantity derived in [35]. This difference comes from whether one chooses to average the axion-induced charge density only over field lines, or also over time. Here, we adopt the former procedure as this yields a smaller back-reaction density, and thus a more conservative estimate of the radio flux.

<sup>8</sup> This is not necessarily true for the polar cap gaps themselves, as the plasma density there is naturally small in the vacuum phase. Nevertheless, this phase is expected to be too short to allow for meaningful resonant conversion, and thus likely will not be impactful in this regard.

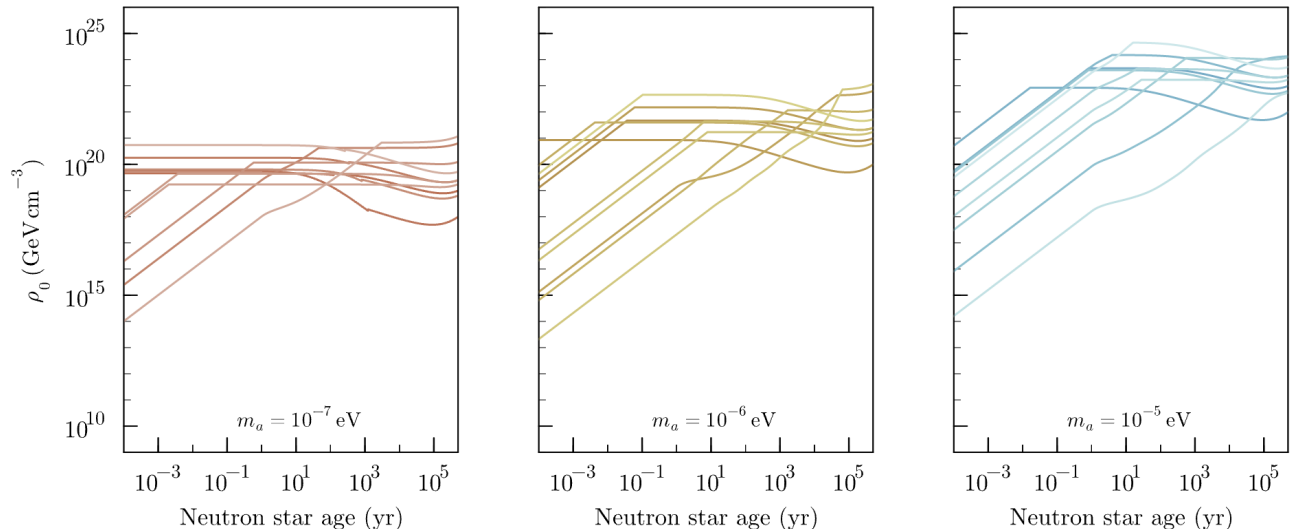


FIG. 3. Axion cloud density at the neutron star surface as a function of neutron star age, plotted for our ten neutron star samples at three different values of the axion mass. The axion-photon coupling is set to  $g_{a\gamma\gamma} = 5 \times 10^{-13} \text{ GeV}^{-1}$ .

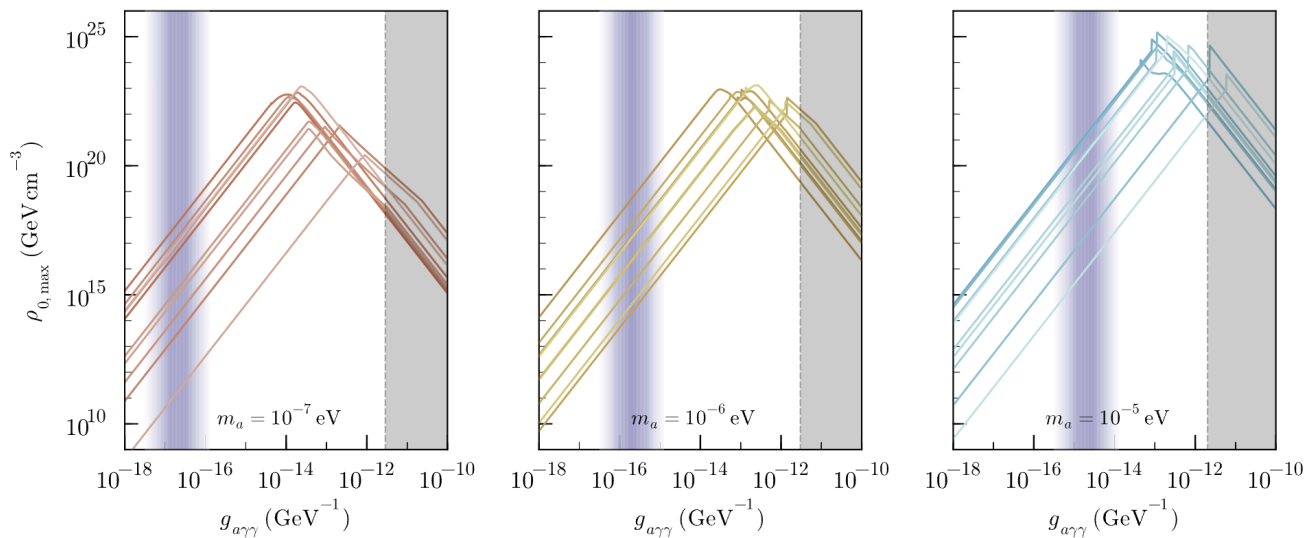


FIG. 4. Maximal axion density achieved at the neutron star surface as a function of axion-photon coupling, plotted for our ten neutron star samples at three different values of the axion mass. The approximate parameter space associated to the QCD axion is shown using vertical purple bands [58]. Previously excluded regions of parameter space [25] are shaded in grey. We note that the behavior at high couplings is a result of truncating the density at  $\rho_{\text{max}}$ , which has been implemented in order to conservatively avoid evolving the axion cloud in the regime where the axion can back-react on the electrodynamics.

conservative predictions of the radio flux<sup>9</sup>). Note, however, that full charge separation is expected to occur in dead neutron stars (see *e.g.* [15]) – we return to the

<sup>9</sup> We have verified using the neutron star parameters at death, that the choice of a spherical conversion surface can suppress the radio flux by as much as four orders of magnitude (although this suppression is significantly reduced for large axion masses, when the conversion surface is generally close to the neutron star surface either way).

implications of this transition in the following section.

Due to the spherical conversion surface, low-energy axions, which are confined to orbits with apoapsis  $r \leq r_c$ , will never dissipate their energy. Higher energy axions, on the other hand, will cross the conversion surface many times, converting with a low probability at each crossing. In order to assess the effect of these resonances on the axion cloud, we identify how frequently resonances are encountered and how efficient each resonance is at depleting the axion cloud. Conversions are anticipated to reach an equilibrium, where the rate of axion injection matches



the rate of energy dissipation – this equilibrium roughly occurs on a timescale  $\tau_{\text{eq}} \sim \tau_{\delta\text{res}} / \langle P_{a \rightarrow \gamma} \rangle$ , where  $\tau_{\delta\text{res}}$  is the timescale between resonant crossings and  $\langle P_{a \rightarrow \gamma} \rangle$  is the typical fraction of axions lost at each crossing.

Fig. 2 shows the reconstructed density profiles of our ten neutron star samples after 1 kyr, adopting fiducial axion parameters  $m_a = 10^{-6}$  eV and  $g_{a\gamma\gamma} = 5 \times 10^{-13}$  GeV $^{-1}$ , and taking the neutron star radius and mass to be  $R_{\text{NS}} = 10$  km and  $M_{\text{NS}} = M_{\odot}$ , respectively. Note that unless otherwise indicated, these values are used as fiducial parameters throughout the text. The dark and light bands reflect the variation across the neutron star population, with the darker bands showing the  $\pm 25\%$  quartiles about the mean, and the lighter bands the minimum/maximum of the population. The density profile exhibits notable dips at radii near  $\mathcal{O}(100)$  km, a result of the fact that energy in the bound states here is being dissipated via resonant photon production. The density profile at smaller radii is unaffected by resonant conversions, and will therefore grow unimpeded. In the absence of conversions, the reconstructed slope outside of the neutron star is found to scale like  $\rho \propto r^{-4}$ <sup>10</sup>.

In order to highlight the importance of  $\rho_{\text{max}}$ , we plot in Fig. 3 the time evolution of the axion energy density at the neutron star surface for three axion masses. Here, each line corresponds to a single neutron star in our sample. Fig. 3 clearly shows sharp interruptions in linear growth of the axion density, reflecting the time at which the axion cloud achieves a surface density equal to  $\rho_{\text{max}}$  (we remind the reader that the maximal density is generally set by the back-reaction density given in Eq. 20). Notice that this saturation can occur across a range of different timescales spanning from  $\tau \ll 10^{-4}$  yrs to  $10^6$  yrs, depending on the axion parameters and neutron star. The non-linear evolution seen in these curves at late times reflects the impact of magneto-rotational spin-down, which can affect both the value of the back-reaction density as well as the axion production rate.

In Fig. 4 we illustrate the scaling of the axion density with axion-photon coupling, plotting the maximal surface density achieved over the course of the neutron star lifetime as a function of  $g_{a\gamma\gamma}$ . For sufficiently large couplings, the back-reaction density in Eq. 20 causes the growth to saturate early in a neutron star’s life; since Eq. 20 scales with  $g_{a\gamma\gamma}^{-2}$ , the maximal density in the axion cloud grows at smaller couplings. There is a turnover (*i.e.* the sharp peaks seen in Fig. 4), however, which for typical neutron stars occurs between  $10^{-14}$  GeV $^{-1} \lesssim g_{a\gamma\gamma} \lesssim 10^{-12}$  GeV $^{-1}$  (also depending on the axion mass)

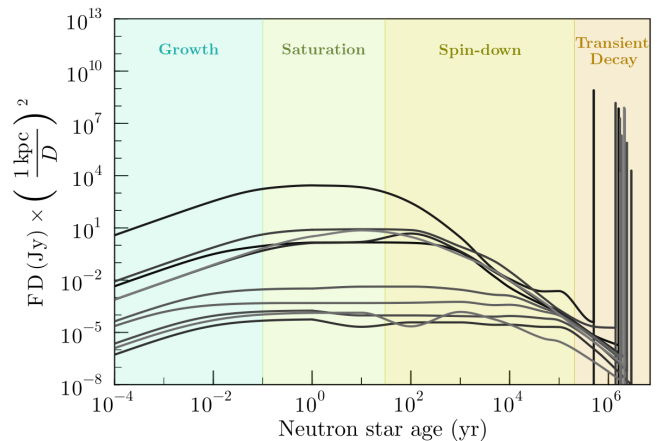


FIG. 5. Temporal evolution of the flux density (produced via resonant axion-photon mixing) from the ten neutron stars in our sample, assuming a distance of 1 kpc. Four emission phases are identified: linear growth, saturation, spin-down, and transient decay (see text for details on the physics driving each evolutionary stage). Results are shown for fiducial values of the axion mass and axion-photon coupling,  $m_a = 10^{-6}$  eV and  $g_{a\gamma\gamma} = 5 \times 10^{-13}$  GeV.

– below this threshold,  $\rho_{\text{max}}$  is not reached within the neutron star’s lifetime, and thus the maximally achieved density in this regime simply scales with  $g_{a\gamma\gamma}^2$ . Fig. 4 highlights two important points. Firstly, there is a general trend that larger axion masses achieve higher densities, however the peak density also tends to occur at larger couplings. Secondly, large axion densities, which exceed the local dark matter density by more than ten orders of magnitude, are achieved at all couplings for the mass range studied here, including *e.g.* QCD axion parameter space (which has been highlighted using the purple band in Fig. 4).

### III. RADIO EMISSION

Sec. II establishes that enormous axion energy densities can be achieved around neutron stars via the gap-production process. The dissipation of this energy via resonant photon production provides a direct observable to probe the existence of axions, namely radio emission. Here we investigate signatures arising from this process, and in Sec. IV we discuss the extent to which they are observable using existing radio infrastructure.

In order to provide a rough understanding of the magnitude and time evolution of the radio flux, we follow the change in the axion production rate and the energy dissipation rate over the lifetime of each of the neutron stars in our sample. Assuming a characteristic distance of 1 kpc and fixing the bandwidth to be the minimal frequency range capturing 95% of the flux (which typically corresponds to 1 – 10 MHz), we show in Fig. 5 the evolution of the flux density for our fiducial parameters. Here we see that, like the axion cloud itself, the radio emis-

<sup>10</sup> Inside the neutron star we instead find that the density is approximately constant. We however caution the reader that in order to extend trajectories inside of the neutron star we have simply applied a re-scaling to the neutron star mass which assumes a constant internal density. In general one should use the internal Schwarzschild metric in this regime, and thus our scaling may not be robust.

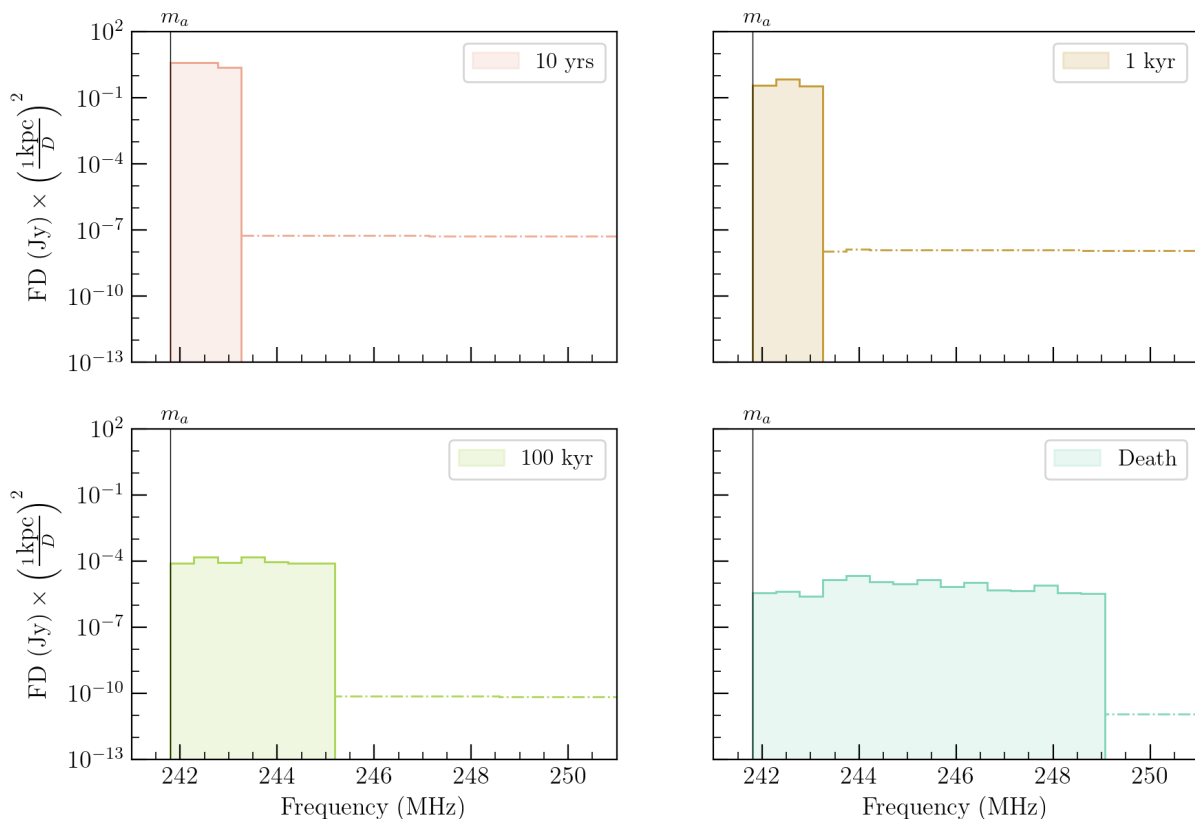


FIG. 6. Spectrum of radio emission generated from axion bound states (solid, filled) and the non-bound axion population (dot-dashed). Results are shown for neutron star 5 (see Table 1) at four different ages. The axion mass and axion-photon coupling are respectively set to  $m_a = 10^{-6}$  eV and  $g_{a\gamma\gamma} = 5 \times 10^{-13}$  GeV $^{-1}$ .

sion of each neutron star undergoes four distinct phases of evolution: growth, saturation, spin-down, and transient decay. We outline the physics driving each of these phases below.

**Growth:** After the neutron star settles into its relaxed state, pair production processes in the polar cap begin producing a non-relativistic population of axions. So long as the axion density remains sufficiently low so that energy dissipation is small, the axion cloud and the radio flux grow linearly with time. In this regime, the radio flux scales proportional to  $g_{a\gamma\gamma}^4$ , with two factors coming from axion production and two coming from resonant conversion. The radio flux traces the evolution of the axion density until the profile equilibrates, a process which occurs at the point when bound state axions are converted with the same intensity as they are injected.

**Saturation:** Once equilibrium is reached, the radio flux and spectrum will remain approximately constant until the neutron star begins to spin-down. Note that the inner part of the density profile does continue to grow, as low-energy axions are not expected to cross resonant conversion surfaces. During this saturation phase, the axion-photon conversion probability becomes *independent* of  $g_{a\gamma\gamma}$  and therefore the radio flux scales as  $g_{a\gamma\gamma}^2$  rather than  $g_{a\gamma\gamma}^4$ . This implies that radio emission

from bound states is amplified relative to the radio emission generated from axions with  $k > k_{\text{esc}}$  (*i.e.* the axion population studied in [25]) by a factor of  $1/\langle P_{a\rightarrow\gamma} \rangle$ . As such, one expects the radio spectrum to be sharply enhanced at frequencies  $m_a \lesssim \omega \lesssim \sqrt{k_{\text{esc}}(r_c)^2 + m_a^2}$ . A secondary distinctive feature in the spectrum arises from the kinematic threshold set by the axion mass – this provides a sharp lower limit for the peaked radio emission. Collectively, these two characteristics serve to produce an overall sharp end-point in the radio spectrum.

We illustrate this in Fig. 6 using one of the sampled neutron stars at various ages. One can see that the radio flux generated by bound states (shaded region) is clearly elevated with respect to the flux produced by axions that escape the magnetosphere (dot-dashed lines). We do note that the instantaneous nature of the transition at the high-frequency edge is a consequence of adopting a perfectly spherical conversion surface, but even in more realistic scenarios the drop is expected to remain sharp. Fig. 6 furthermore shows that both the width and amplitude of the spectral feature evolve over the course of the neutron star’s life – this is a direct consequence of the fact that magneto-rotational spin-down shifts the conversion surface to smaller radii while simultaneously decreasing the injection rate of axions, modifying both

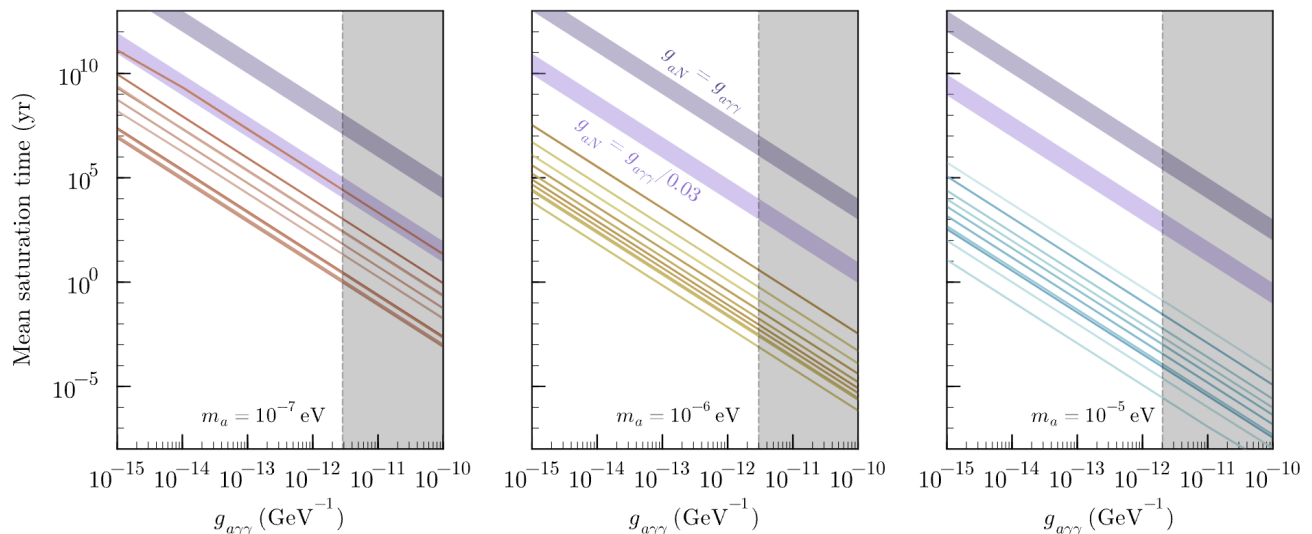


FIG. 7. Mean saturation time (*i.e.* the average time it takes before the axions that contribute to the resonant flux have a conversion rate equal to 90% of their production rate) as a function of axion-photon coupling, plotted for our ten neutron star samples at three different values of the axion mass. Previously excluded regions of parameter space [25] are shaded in grey. For comparison, we also show for each neutron star the mean absorption timescale (*i.e.* the average time it takes before 90% of produced axions are being absorbed inside of the neutron star) for axions whose apoapsis is fixed to the conversion radius – to avoid clutter, this is displayed as a band, rather than ten individual lines. Absorption timescales are shown for two characteristic ratios of  $g_{aN}/g_{a\gamma\gamma}$ , one corresponding to equality and the other to the ratio for the QCD axion in the KSVZ model (see *e.g.* [59]).

the frequency and characteristic conversion probability of produced photons.

The characteristic time required in order to reach saturation depends on both the axion mass and the axion-photon coupling; we provide an estimation of this saturation time in Fig. 7. This figure shows that saturation is not guaranteed to occur for sufficiently small couplings, as neutron stars may not always reach equilibrium before crossing the death line. We also plot in Fig. 7 the typical axion-nucleon bremsstrahlung absorption timescale,  $\tau_{90}$ , adopting an axion-nucleon coupling of  $g_{aN} = g_{a\gamma\gamma}$  (dark purple) and  $g_{aN} = g_{a\gamma\gamma}/0.03$  (light purple), the latter roughly corresponding to the expected ratio in the KSVZ model – these curves illustrate that axion absorption is generally insubstantial compared to resonant axion-photon mixing, and thus unlikely to be important in the evolution of the axion cloud.

**Spin-down:** Magneto-rotational decay of the neutron star causes the rotational period to increase and the magnetic field to decrease. This leads to two counteracting effects:

- The characteristic charge density in the magnetosphere tends to decrease, implying a shift in the resonant conversion radius to smaller values where axion densities are larger. This serves to increase the radio flux.
- The production rate of axions tends to decrease, which translates to a decrease in the radio flux.

We have found that the latter effect generally controls the long term evolution of the flux density, resulting in a diminishing flux as a function of neutron star age during this phase. Nevertheless, small deviations from this trend can occur, as seen in Fig. 5.

**Transient Decay:** The magnetospheres of dead neutron stars are known to relax to the so-called electro-sphere solution (also referred to as the disk-dome solution), which is a fully charge-separated state that resembles the GJ model near the surface of the neutron star but falls off more quickly at large radii (see *e.g.* [15]).

Within this solution, regions of vacuum open in between the regions of positive and negative charges (extending all the way to the neutron star surface), allowing for axions of all energies (*i.e.* at all radii) to resonantly convert to radio photons. Since pair production processes are no longer efficient in the polar caps of dead neutron stars, axion production is furthermore expected to cease. This implies that all residual energy stored in the axion cloud will dissipate – in other words, dead neutron stars *typically* do not have axion clouds<sup>11</sup>. Assuming that vacuum regions near the neutron star surface open on the

<sup>11</sup> For axion masses  $m_a \geq 10^{-5}$  eV we find that in some cases the conversion surface shrinks below the neutron star radius before the magnetosphere charge separates; if this happens there will be no transient phase, and the neutron star will be left with a residual axion cloud that slowly dissipates via non-resonant mixing (for which the decay timescale can be quite sizable, see *e.g.* [35]).

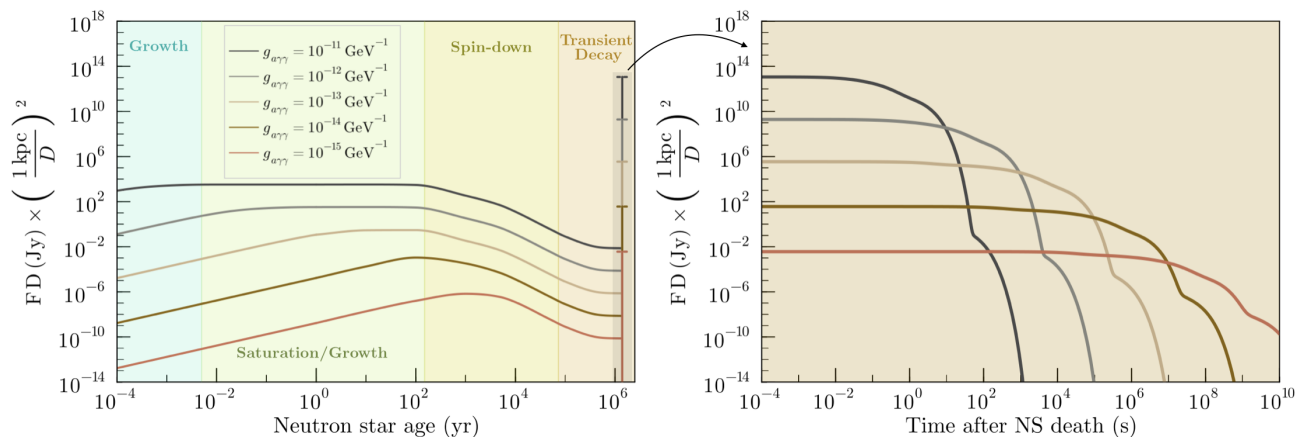


FIG. 8. *Left*: Temporal evolution of the flux density (produced via resonant axion-photon mixing) from neutron star 5 (see Table 1), plotted as a function of axion-photon coupling. The emission phases are the same as in Fig. 5. *Right*: Zoom-in on the transient burst. The axion mass is set to  $m_a = 10^{-6}$  eV.

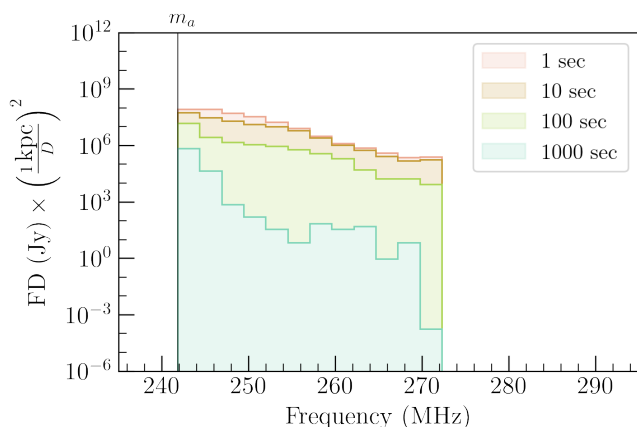


FIG. 9. Transient spectrum of neutron star 5 (see Table 1) at four different times after charge separation (assumed to occur instantaneously when the neutron star crosses the death line). The axion mass and axion-photon coupling are respectively set to  $m_a = 10^{-6}$  eV and  $g_{a\gamma\gamma} = 5 \times 10^{-13}$  GeV $^{-1}$ .

light crossing time, the timescale over which energy dissipates can be rapid, potentially generating a transient burst or perhaps a slower transient decay. The exact properties of the transient phase depend heavily on the axion mass, axion-photon coupling, and the strength of the neutron star's magnetic field.

Here, we model the transient by assuming the plasma density near the neutron star relaxes approximately instantaneously (*i.e.* within the light-crossing time of the magnetosphere) to the charge-separated GJ charge density, given by

$$n_{\text{GJ}} \simeq \frac{2\vec{B}_0 \cdot \vec{\Omega}_{\text{NS}}}{e}. \quad (23)$$

Using the traced trajectories, and assuming the axion production mechanism has been abruptly turned off, we

subsequently determine the rate at which energy is dissipated from the cloud. For large masses and couplings, this process may dissipate the entire axion cloud over timescales on the order of a second, while at lower masses and couplings the transient phase may last more than thousands of years. The temporal evolution of the transient as a function of coupling is illustrated for a particular neutron star in Fig. 8. In general, one expects the peak flux density during the transient phase to scale as  $g_{a\gamma\gamma}^4$  (since larger couplings imply both a larger axion density and faster energy dissipation). However, for sufficiently large couplings one may enter the adiabatic regime in which the conversion probability saturates to  $P_{a \rightarrow \gamma} \sim 1$ , softening the functional dependence on the coupling. For completeness, we also plot the evolution of the transient spectrum in Fig. 9 using the same parameters and pulsar as in Fig. 8. Here, one can see that the transient burst occurs over a narrow window of frequencies and contains a slight spectral tilt, peaking near the axion mass.

The transient duration, defined here to be the time over which 90% of the energy is dissipated, is shown for each of our neutron stars in Fig. 10 as a function of axion-photon coupling. Notice first of all that at  $m_a = 10^{-5}$  eV most neutron stars do not experience the transient event – this is because the characteristic plasma density at death is well below the axion mass. Fig. 10 also shows the presence of multiple spectral breaks, causing the curves to deviate from a simple power-law scaling – at large masses this occurs when the conversion becomes adiabatic (*i.e.*  $P_{a \rightarrow \gamma}$  approaches order one values), while at small masses the double-break feature arises because there exist two sub-populations within the axion cloud (differentiated by the sharp dip in the density profile, see Fig. 2) which dissipate their energy on different timescales.

Having described the general spectral features in the radio band that are expected to arise from the evolution

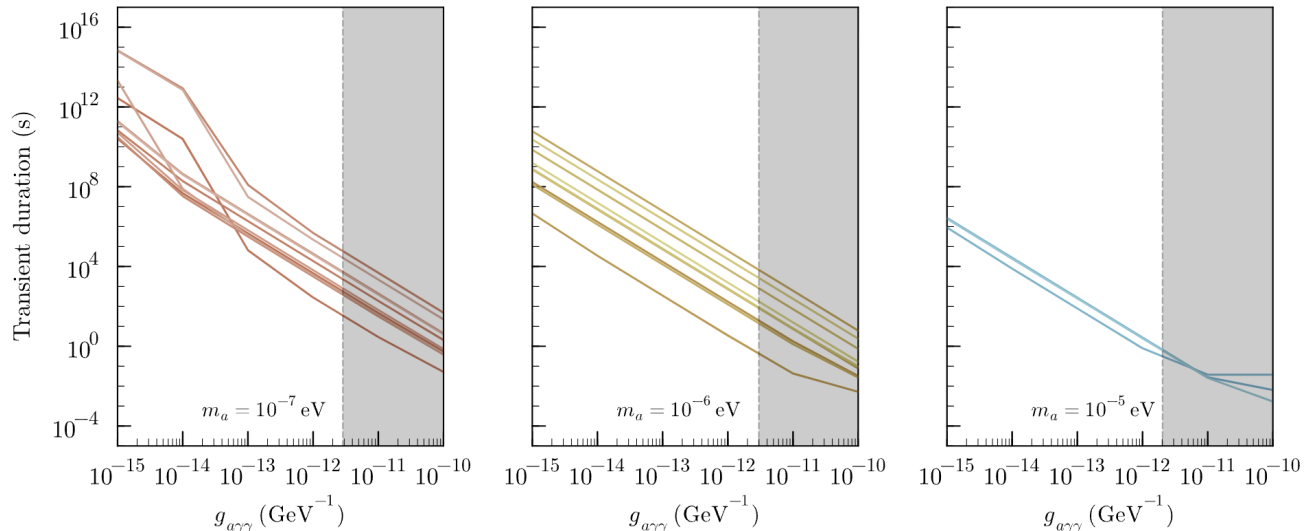


FIG. 10. Transient duration as a function of axion-photon coupling, plotted for our ten neutron star samples at three different values of the axion mass. At  $m_a = 10^{-5}$  eV only three neutron stars are shown because the other samples do not produce a transient (as a result of their conversion surface shrinking below the neutron star radius before magnetosphere charge separation). Previously excluded regions of parameter space [25] are shaded in grey.

of axion clouds, we now turn our attention to the extent to which these features are observable. We caution the reader that these projections should be interpreted with care; despite the fact that we expect the qualitative evolution of these systems to be relatively robust, the choices made to describe the pulsar population and the evolution of the charge distribution can alter the quantitative estimates performed here. We reserve a more thorough investigation into the impact of these systematics on the projected sensitivity for future work.

#### IV. SENSITIVITY

The radio flux from a pulsar observed on Earth is given by  $F = dP/d\Omega/D^2$ , where  $dP/d\Omega$  is the differential power emitted from the pulsar along the line-of-sight and  $D$  is the distance to the pulsar. Sensitivity of radio telescopes is often quoted in terms of flux density, defined as  $S = F/\Delta\nu$ , where  $\Delta\nu$  is the signal bandwidth. The minimum detectable flux density for a given signal-to-noise ratio (SNR) of a single radio telescope is given by (see *e.g.* [60])

$$S_{\min} = \text{SNR} \times \frac{T_{\text{sys}}}{G\sqrt{N_{\text{pol}}\tau\Delta\nu}}. \quad (24)$$

Here  $T_{\text{sys}}$  is the system temperature, which accounts for all sources of astrophysical backgrounds and receiver noise. The telescope ‘gain’,  $G$ , describes the effective collecting area of the telescope,  $N_{\text{pol}}$  is the number of polarization states being observed, and  $\tau$  is the signal integration time. Radio telescope arrays combine observations from many telescopes by correlating the obser-

vations along the independent baselines established by  $N_{\text{tele}}$  independent instruments; collectively, this procedure allows for an enhancement in sensitivity set by (see *e.g.* [61])

$$S_{\min}^{\text{array}} = \frac{S_{\min}}{\sqrt{\frac{1}{2}N_{\text{tele}}(N_{\text{tele}} - 1)}}. \quad (25)$$

We use Eqs. 24 and 25 to compute the minimum observable flux densities for both continuous and transient emission. We emphasize that we use the term ‘transient’ to describe radio emission from axion cloud decay at neutron star death, although the duration may be considerably longer than the total observing time of the radio emission (see Fig. 10). When considering the minimum flux density for a transient, we take  $\tau = \text{Min}[\tau_{\text{dur}}, \tau_{\text{obs}}]$ , where  $\tau_{\text{dur}}$  is the transient duration and  $\tau_{\text{obs}}$  is the total observation time. For the axion masses considered in this paper,  $m_a = 10^{-7}$  eV,  $10^{-6}$  eV, and  $10^{-5}$  eV (corresponding to frequencies of 24 MHz, 240 MHz, and 2.4 GHz), we estimate the sensitivity using the Low Frequency Array (LOFAR; used for sensitivity at 24 MHz), the Murchison Widefield Array (MWA; used for sensitivity at 240 MHz), and the Green Bank Telescope (GBT; used for sensitivity at 2.4 GHz), respectively. The system temperature is set to be a combination of the intrinsic receiver noise and the sky temperature, *i.e.*  $T_{\text{sys}} = T_{\text{rec}} + T_{\text{sky}}$ . Here

$$T_{\text{sky}} = T_{\text{sky},0} \left( \frac{\nu}{\nu_0} \right)^\gamma \quad (26)$$

is normalized to the observations by the ARCADE 2 collaboration [93],  $T_{\text{sky},0} = (24.1 \pm 2.1)$  K,  $\nu_0 = 310$  MHz,

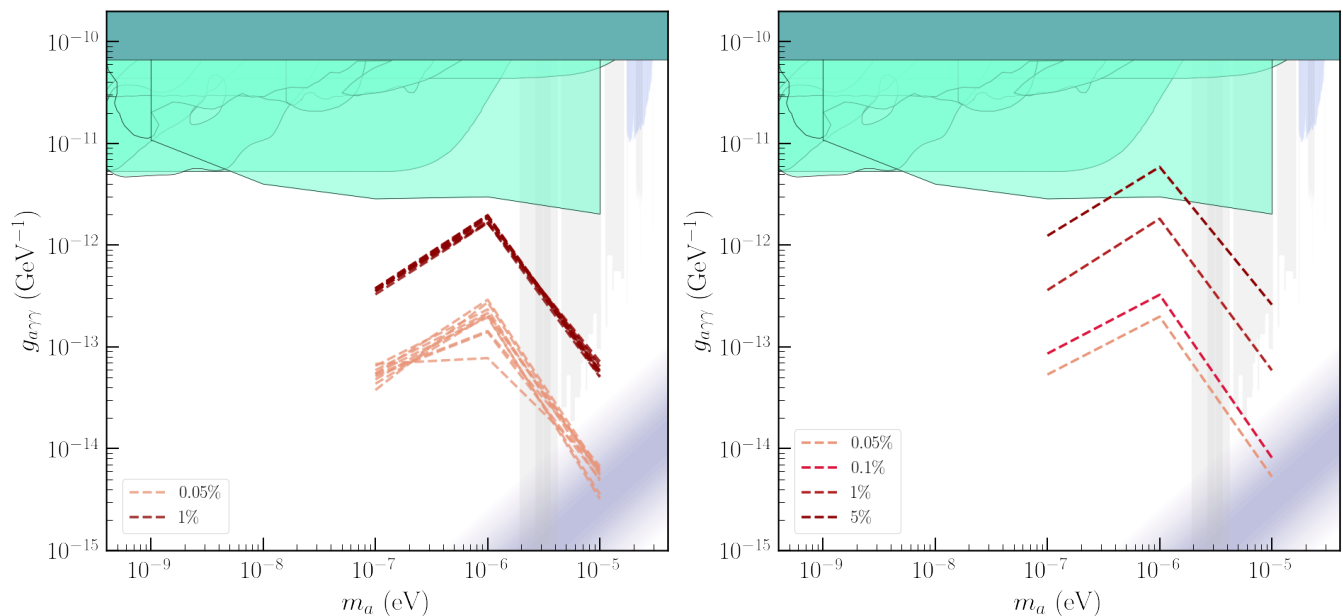


FIG. 11. Projected sensitivity to the radio end-point arising due to resonant photon production from axion bound states. *Left:* We plot the projections from ten different realizations of our population simulation, requiring either 0.05% or 1% of the neutron star population to have flux density above threshold. *Right:* We instead plot the average projected sensitivity across the ten populations, further varying the required number of observable neutron stars. Our projections are compared to current constraints from neutron stars [21] (shown in blue), haloscopes [62–79] (grey), helioscopes [80] (teal), and astrophysics [25, 81–92] (light green). The first two of these categories are drawn with reduced opacity to highlight that they require axions to be dark matter. The QCD axion band is shown in purple. [58]

and  $\gamma = -2.599 \pm 0.036$ . The combination  $T_{\text{sys}}/G$  (which depends on the frequency and the instrument) is called the system equivalent flux density (SEFD). The sensitivity of LOFAR at  $\nu = 30$  MHz is SEFD  $\approx 89$  kJy [94], for MWA at  $\nu = 250$  MHz is SEFD  $\approx 60$  kJy [95], and for GBT at  $\nu = 2.4$  GHz is SEFD  $\approx 10$  Jy [96]<sup>12</sup>. LOFAR is comprised of 52 stations, MWA of 128 observing elements, and GBT is a 100-m single dish telescope. Taking  $N_{\text{pol}} = 2$ , fixing the observing time to be 1 hour, and setting the bandwidth to be  $0.05 \times m_a$  (roughly the maximal width of the features of interest), the requirement of an SNR level of 5 corresponds to minimum observable flux densities of  $S_{\text{min}}(24 \text{ MHz}) \sim 100$  mJy,  $S_{\text{min}}(240 \text{ MHz}) \sim 10$  mJy, and  $S_{\text{min}}(2.4 \text{ GHz}) \sim 0.09$  mJy. We use these values to estimate the sensitivity to continuous and transient emission in Figs. 11 and 13 respectively (except in the cases where the transient duration is shorter than an hour; here we compute with a smaller observing time).

### A. Kinematic End-Point

First, we turn our attention to estimating the sensitivity of existing radio telescopes to the radio end-point shown in Fig. 6, which we achieve by simulating the population of neutron stars within our Milky Way galaxy.

Neutron stars form from the collapse of main-sequence stars with  $8 M_{\odot} \lesssim M \lesssim 25 M_{\odot}$ . The core-collapse supernova (CCSNe) rate in the galaxy is thought to be on the order of two per century – since most CCSNe result in the formation of a neutron star (with just a small fraction going into black holes), we adopt a maximally conservative estimate of the neutron star formation rate of  $\dot{N}_{\text{NS}} = 1/100$  yrs (taken for simplicity to be constant over the history of the Milky Way). We further assume that the spatial distribution of neutron stars follows the galactic disk (which we take to extend out to a distance of 10 kpc), and that any neutron star older than  $10^6$  yrs has crossed the death line (and is thus no longer producing continuous emission). This generates a population of  $\sim 10^4$  active neutron stars with ages  $\tau_1, \dots, \tau_N$ . The properties of each neutron star in the simulated population is taken to be one of the sample neutron stars listed in Table 1 (the assignment being done at random), but evaluated at the appropriate age  $\tau_i$ .

We compute the flux density in the radio end-point for each of the neutron stars in ten different realizations of the Milky Way population, and determine the cou-

<sup>12</sup> The GBT sensitivity can also be determined using the online sensitivity calculator, found [here](#). We find that this yields a slightly more conservative estimate, and thus we adopt a slightly larger SEFD of 17 Jy in order to correct for this difference.

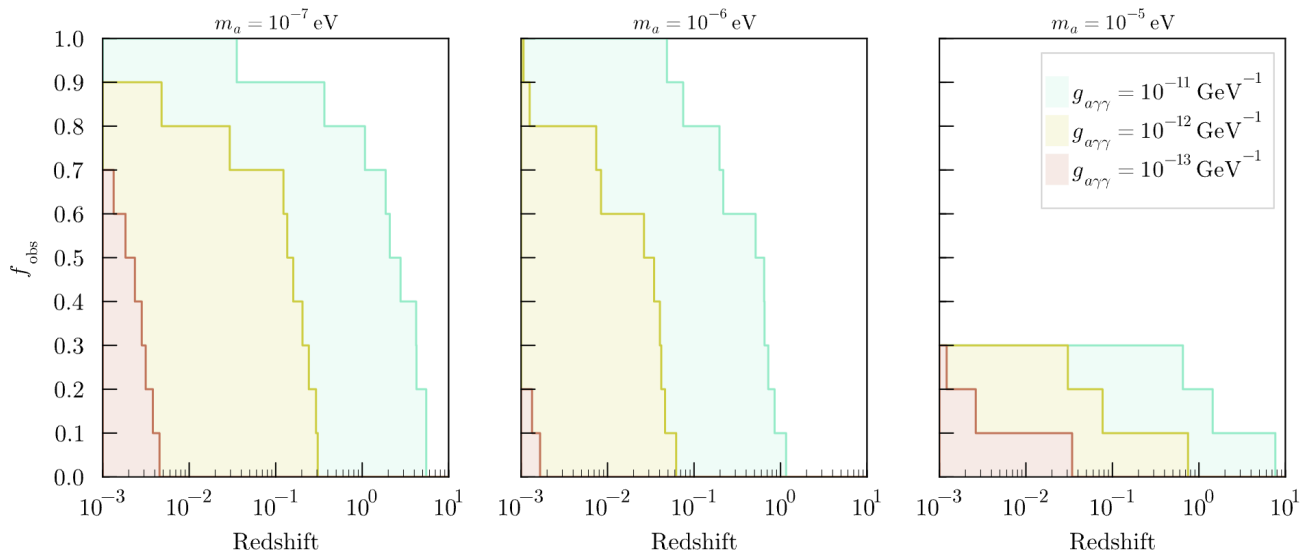


FIG. 12. Fraction of observable transient events as a function of redshift and axion-photon coupling, plotted at three different values of the axion mass. At  $m_a = 10^{-5}$  eV we do not find values for  $f_{\text{obs}}$  above 0.3, since at this mass only three of our neutron star samples produce a transient. We assume detection thresholds as calculated at the start of Sec. IV.

pling for which the flux of at least either 5 or 100 stars (corresponding to 0.05% and 1% of the total population respectively) exceeds the flux density thresholds outlined in the previous section<sup>13</sup>. The projections determined using this procedure are shown in the left panel of Fig. 11, where each line corresponds to a different realization of the neutron star population. In the right panel of Fig. 11 we further illustrate the change in sensitivity as we shift the minimum number of observable neutron stars, taking on values between 0.05% and 5% of the total population. The lines shown in this panel reflect the average sensitivity realized over the ten simulated populations. In all simulations we find that the neutron stars with the largest flux densities have distances neither particularly close nor particularly far from Earth. The populations are furthermore not dominated by any single neutron star in our sample (rather, five of the neutron stars tend to produce overall stronger fluxes than the others). We do note, however, that the best projections are generally set by younger neutron stars, having ages  $1 \text{ kyr} \lesssim \tau_i \lesssim 10 \text{ kyrs}$ . At larger couplings, when neutron stars are more abundant, older neutron stars that are closer to Earth can instead dominate the signal.

## B. Transient Decay

In this section we assess the observability of transient events, working under the assumption that each neutron star undergoes a single transient decay which occurs instantly when crossing the death line. This is likely an oversimplification. It is unclear how quickly neutron stars will evolve from the active to the dead state, and also whether transients can be induced earlier in a neutron star's lifetime from temporary rearrangements of charges in the magnetosphere. Such short-term changes in the magnetospheres of young pulsars can for example arise when the star experiences a glitch, *i.e.* a sudden spin-up that is expected to occur when angular momentum is exchanged between the super-fluid interior and the solid crust, see *e.g.* [97]<sup>14</sup>. As a result, the sensitivity to the transient decay feature is expected to be notably more uncertain than that of the kinematic end-point. Nevertheless, given that the energy near the neutron star surface must be dissipated, we expect that the calculations performed here still provide reasonable benchmark estimates that also hold in more general scenarios.

In order to estimate the observability of transient decays one must know the transient event rate, since

<sup>13</sup> Note that in general the observation of a single spectral line could be sufficient in order to detect axions. We adopt more conservative thresholds for two reasons: (i) our population modeling is highly uncertain, and thus adopting different thresholds indirectly reflects the sensitivity to this aspect of the analysis, and (ii) the joint detection of this feature in multiple neutron stars across the population would provide striking evidence for the existence of axions.

<sup>14</sup> It is worth highlighting that glitches are expected to induce sizable shifts in the resonant conversion surface on timescales comparable to the light crossing time. Such a shift could open resonant conversions in parts of the cloud which had previously been kinematically blocked, leading to a rapid dissipation of radio energy on  $\mathcal{O}(\text{ms})$  timescales. It is conceivable that such rapid bursts can contribute to the observable population of fast radio bursts (FRBs); we leave a more detailed investigation of this phenomenon to future work.

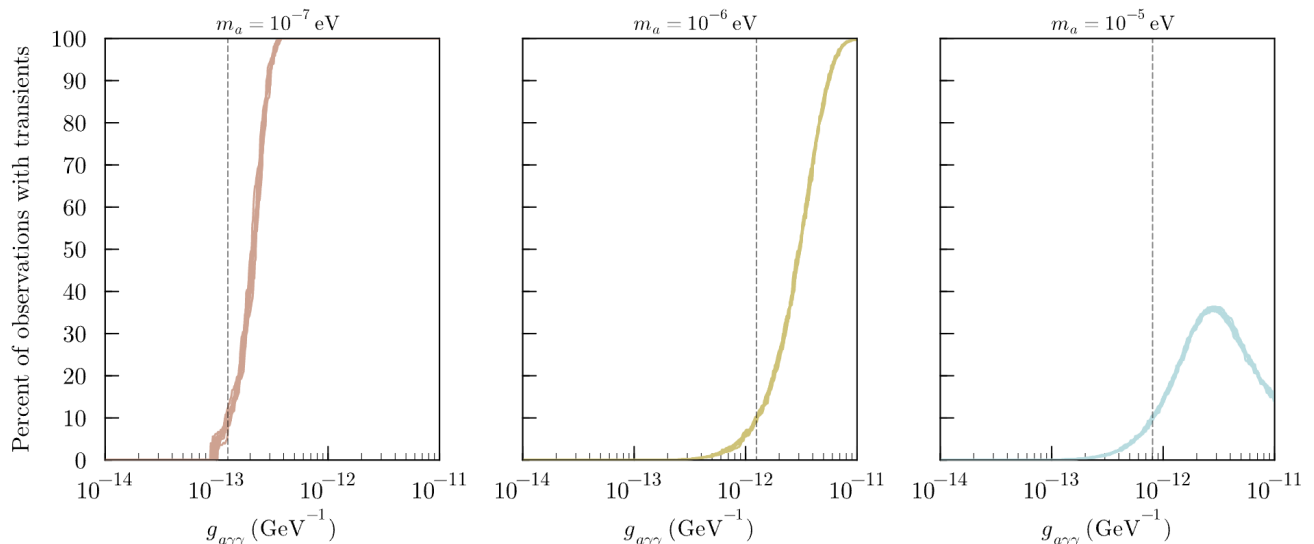


FIG. 13. Percentage of observations within our observation scheme that contain at least one transient event. Results are shown for three fixed axion masses as a function of axion-photon coupling. The thickness of the bands reflect the impact of generating ten different realizations of the observing procedure. The vertical dashed line highlights the coupling at which 10% of observations contain a transient.

this effectively defines the typical distances of transients from Earth. The lifetime of progenitor main sequence stars,  $\tau_{\text{CC}} \approx 55 \text{ Myr} (M/8 M_{\odot})^{-2.5}$ , and the characteristic timescale required for neutron stars to cross the death line,  $\tau_{\text{NS}} \approx 10 \text{ Myr}$ , are negligible on cosmological timescales. As a result, we can assume the transient rate follows the cosmological CCSNe rate,  $R_{\text{CC}}(z) = \xi \psi(z)$ . Here  $\psi(z)$  is the star formation rate and  $\xi = 6.8 \times 10^{-3} M_{\odot}^{-1}$  is the efficiency to form CCSNe, which we compute using the Salpeter initial mass function. For  $\psi(z)$  we adopt the best-fit function to UV and IR galaxy surveys derived in [98], giving us a CCSNe rate of

$$R_{\text{CC}}(z) \simeq 10^{-4} \text{ yr}^{-1} \text{ Mpc}^{-3} \frac{(1+z)^{2.7}}{1 + [(1+z)/2.9]^{5.6}}. \quad (27)$$

Only a fraction,  $f_{\text{obs}}$ , of transients will be observable from redshift  $z$ . Here, we estimate this as the fraction of our ten sampled pulsars that would have a peak transient flux density above the thresholds defined at the start of this section. We plot  $f_{\text{obs}}$  as a function of redshift and axion mass in Fig. 12 for various axion-photon couplings; here we have neglected the impact of red-shifting of the central frequency, as for the couplings of interest observable transients tend to be concentrated toward low redshifts where this effect is negligible. It is worth mentioning that our estimates of  $f_{\text{obs}}$  are based on a small population of only ten samples – it is possible that a small number of rare events (with  $f_{\text{obs}} \ll 10\%$ ) actually dominate the total event rate, since such events could be observable to much larger distances. The computational complexity of evaluating transient events for large populations of neutron stars unfortunately makes estimating the tails of this distribution currently unfeasible, and so

we defer a more detailed study of a larger population to future work.

The observable transient rate (OTR) can be obtained by combing Eq. 27 with the results shown in Fig. 12, and is given by

$$\dot{N}_{\text{obs}}(g_{a\gamma\gamma}) \simeq \int dV_c f_{\text{obs}}(z, g_{a\gamma\gamma}) R_{\text{CC}}(z), \quad (28)$$

where  $dV_c = (1+z)^2 D_A(z)^2 / H(z) d\Omega dz$  is the comoving volume element,  $D_A(z)$  is the angular diameter distance, and  $H(z)$  is the Hubble parameter. Eq. 28 describes the rate at which transient decays are observable across the full sky – radio telescopes, however, only observe a fraction of the sky, and only for a fraction of the day. In order to establish a notion of transient observability based off of Eq. 28, we therefore devise a demonstrative observation scheme. Namely, we: (i) choose a sufficiently large observing window (so that for each axion mass and axion-photon coupling  $\tau_{\text{window}} \gg \dot{N}_{\text{obs}}^{-1}, \tau_{\text{dur}}$ ), (ii) populate this window randomly with  $\langle N \rangle = \tau_{\text{window}} \times \dot{N}_{\text{obs}}$  transient events, (iii) sample  $10^3$  random observation times within the observation window (each assumed to have a duration of 1 hour), and finally (iv) record the percentage of these observations that contain at least one observable transient event.

We perform ten realizations of the above procedure at a range of axion-photon couplings for axion masses  $10^{-7} - 10^{-5} \text{ eV}$ . The results are plotted in Fig. 13. The observation scheme itself is furthermore illustrated in Fig. 14 for a single choice of parameters. Interestingly, we find that at  $m_a = 10^{-5} \text{ eV}$  the percentage of observations with a transient never saturates and instead drops at large couplings – this is a consequence of the fact that



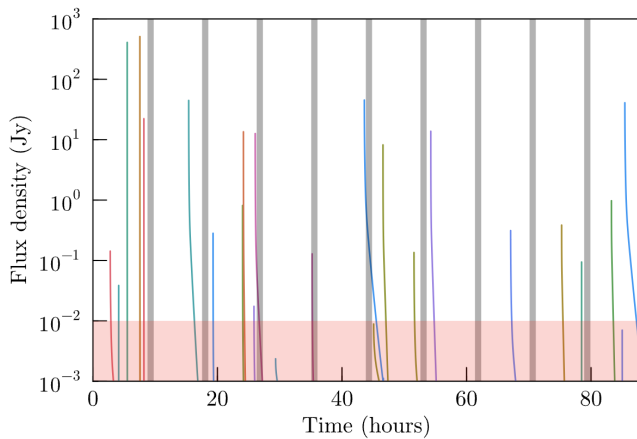


FIG. 14. Illustration of the observational procedure used to generate the results in Fig. 13. Here, transient events are randomly distributed over the observing window  $\tau_{\text{window}}$ . The grey vertical bands illustrate the characteristic observing times (for the purpose of illustration, we have chosen to plot 1% of total observations, and have taken these to be regularly spaced), and the flux threshold is highlighted in red; observable transients are thus identified as those which cross the grey bands while remaining above the red band (as mentioned earlier, for transients shorter than the observing time the flux threshold is actually higher – this is taken into account, but not indicated in the plot). This illustration has been made using an axion mass and coupling of  $m_a = 10^{-6}$  eV and  $g_{a\gamma\gamma} = 10^{-12}$  GeV $^{-1}$ .

the duration of transients becomes relatively short in this part of axion parameter space.

The procedure outlined above does not account for the fact that radio telescopes only view a small fraction of the sky (for example, LOFAR has a full width at half maximum on the order of a few degrees). In order to correct for this we note that typical telescopes observe  $\sim 5000$  hours per year, with many having been in operation for more than a decade. Assuming for a moment that there exists one observable event in every hour of observation, one would expect LOFAR to have observed on the order of  $(0.006 \text{ str}/4\pi \text{ str}) \times 1 \text{ event/hour} \times 5000 \text{ hours/year} \times 16 \text{ years} \sim 38$  events. At small couplings, however, the fraction of observable events per one hour of observing time is significantly reduced (see Fig. 13). We choose to estimate the detection threshold as the coupling for which  $\mathcal{O}(10\%)$  of observations have a transient present in the sky – in the case of LOFAR, this would correspond to roughly  $\sim 4$  observed events. Our detection thresholds are highlighted in Fig. 13 using vertical dashed lines.

## V. CONCLUSIONS

In this manuscript we have shown that if there exists an axion with mass in the range  $10^{-9}$  eV  $\lesssim m_a \lesssim 10^{-4}$  eV that couples to electromagnetism, then all active neu-

tron stars are expected to be surrounded by dense axion clouds. This is an inescapable consequence of the fact that non-relativistic axions can be copiously produced in the polar caps of neutron stars and gravitationally bound to the star. Owing to their feeble interactions, these bound state axions struggle to dissipate their energy, leading to substantial growth of the local axion density on astrophysical timescales.

Using a synthesized population of neutron stars, we have shown that the typical densities of the axion cloud near the surface of the neutron star can easily reach and exceed  $10^{22}$  GeV cm $^{-3}$ , generating environments in which the large axion number densities can compensate for the feeble nature of their interactions with the Standard Model. We have also demonstrated that the axion cloud will, for most axion masses and axion-photon couplings, generate radio emission via resonant axion-photon mixing. Like the cloud itself, this radio emission evolves through four phases over the course of the neutron star lifetime, generating multiple distinct signatures. These notably include a sharp end-point in the radio spectrum (roughly centered about the axion mass and with a width on the order of a few percent), and transient lines generated from the reconfiguration of charges in the magnetosphere (these can either occur during a pulsar glitch, or at the end of a neutron star’s lifetime when charges in the magnetosphere separate). Importantly, the quoted densities at high couplings  $g_{a\gamma\gamma} \gtrsim 10^{-14}$  GeV $^{-1}$  have been conservatively truncated when the back-reaction of the axion on the electrodynamics becomes relevant – while this is believed to be conservative, a more detailed numerical treatment of this regime will be necessary in order to better understand the properties of axion clouds in this region of parameter space.

The existence of axion clouds opens up a number of new phenomenological probes for axions in the mass range  $10^{-9}$  eV  $\lesssim m_a \lesssim 10^{-4}$  eV, all with strong discovery potential, motivating further investigation into the behavior of dense axion clouds around neutron stars.

## VI. ACKNOWLEDGMENTS

The authors would like to thank Ken Van Tilburg, Andrea Caputo, and Georg Raffelt for their valuable discussions. DN and CW are supported by the European Research Council (ERC) under the European Union’s Horizon 2020 research and innovation programme (Grant agreement No. 864035 - Undark). AP acknowledges support from the Princeton Center for Theoretical Science. SJW acknowledges support through the program Ramón y Cajal (RYC2021-030893-I) of the Spanish Ministry of Science and Innovation, and through the European Research Council (ERC) under the European Union’s Horizon 2020 research and innovation programme (Grant agreement No. 864035 Undark) and the Netherlands eScience Center, grant number ETEC.2019.018.

- 
- [1] R. D. Peccei and H. R. Quinn, *Phys. Rev. Lett.* **38**, 1440 (1977).
- [2] R. D. Peccei and H. R. Quinn, *Phys. Rev. D* **16**, 1791 (1977).
- [3] S. Weinberg, *Phys. Rev. Lett.* **40**, 223 (1978).
- [4] F. Wilczek, *Phys. Rev. Lett.* **40**, 279 (1978).
- [5] A. Arvanitaki, S. Dimopoulos, S. Dubovsky, N. Kaloper, and J. March-Russell, *Phys. Rev. D* **81**, 123530 (2010), [arXiv:0905.4720 \[hep-th\]](#).
- [6] E. Witten, *Phys. Lett. B* **149**, 351 (1984).
- [7] M. Cicoli, M. Goodsell, and A. Ringwald, *JHEP* **10**, 146 (2012), [arXiv:1206.0819 \[hep-th\]](#).
- [8] J. P. Conlon, *JHEP* **05**, 078 (2006), [arXiv:hep-th/0602233](#).
- [9] P. Svrcek and E. Witten, *JHEP* **06**, 051 (2006), [arXiv:hep-th/0605206](#).
- [10] C. B. Adams *et al.*, in *Snowmass 2021* (2022) [arXiv:2203.14923 \[hep-ex\]](#).
- [11] M. S. Pshirkov and S. B. Popov, *J. Exp. Theor. Phys.* **108**, 384 (2009), [arXiv:0711.1264 \[astro-ph\]](#).
- [12] A. Hook, Y. Kahn, B. R. Safdi, and Z. Sun, *Phys. Rev. Lett.* **121**, 241102 (2018), [arXiv:1804.03145 \[hep-ph\]](#).
- [13] G.-y. Huang, T. Ohlsson, and S. Zhou, *Phys. Rev.* **D97**, 075009 (2018), [arXiv:1712.04792 \[hep-ph\]](#).
- [14] M. Leroy, M. Chianese, T. D. P. Edwards, and C. Weniger, *Phys. Rev. D* **101**, 123003 (2020), [arXiv:1912.08815 \[hep-ph\]](#).
- [15] B. R. Safdi, Z. Sun, and A. Y. Chen, *Phys. Rev. D* **99**, 123021 (2019), [arXiv:1811.01020 \[astro-ph.CO\]](#).
- [16] R. A. Battye, B. Garbrecht, J. I. McDonald, F. Pace, and S. Srinivasan, *Phys. Rev. D* **102**, 023504 (2020), [arXiv:1910.11907 \[astro-ph.CO\]](#).
- [17] J. W. Foster *et al.*, *Phys. Rev. Lett.* **125**, 171301 (2020), [arXiv:2004.00011 \[astro-ph.CO\]](#).
- [18] S. J. Witte, D. Noordhuis, T. D. Edwards, and C. Weniger, *Physical Review D* **104** (2021), [10.1103/physrevd.104.103030](#).
- [19] A. J. Millar, S. Baum, M. Lawson, and M. C. D. Marsh, *J. Cosmology Astropart. Phys.* **2021**, 013 (2021), [arXiv:2107.07399 \[hep-ph\]](#).
- [20] R. A. Battye, J. Darling, J. McDonald, and S. Srinivasan, “Towards robust constraints on axion dark matter using psr j1745-2900,” (2021), [arXiv:2107.01225 \[astro-ph.CO\]](#).
- [21] J. W. Foster, S. J. Witte, M. Lawson, T. Linden, V. Gajjar, C. Weniger, and B. R. Safdi, (2022), [arXiv:2202.08274 \[astro-ph.CO\]](#).
- [22] S. J. Witte, S. Baum, M. Lawson, M. C. D. Marsh, A. J. Millar, and G. Salinas, *Phys. Rev. D* **107**, 063013 (2023), [arXiv:2212.08079 \[hep-ph\]](#).
- [23] R. A. Battye, M. J. Keith, J. I. McDonald, S. Srinivasan, B. W. Stappers, and P. Weltevrede, (2023), [arXiv:2303.11792 \[astro-ph.CO\]](#).
- [24] A. Prabhu, *Phys. Rev. D* **104**, 055038 (2021), [arXiv:2104.14569 \[hep-ph\]](#).
- [25] D. Noordhuis, A. Prabhu, S. J. Witte, A. Y. Chen, F. Cruz, and C. Weniger, (2022), [arXiv:2209.09917 \[hep-ph\]](#).
- [26] A. Iwazaki, *Phys. Rev. D* **91**, 023008 (2015), [arXiv:1410.4323 \[hep-ph\]](#).
- [27] Y. Bai and Y. Hamada, *Phys. Lett. B* **781**, 187 (2018), [arXiv:1709.10516 \[astro-ph.HE\]](#).
- [28] T. Dietrich, F. Day, K. Clough, M. Coughlin, and J. Niemeyer, *Mon. Not. Roy. Astron. Soc.* **483**, 908 (2019), [arXiv:1808.04746 \[astro-ph.HE\]](#).
- [29] A. Prabhu and N. M. Rapidis, *JCAP* **10**, 054 (2020), [arXiv:2005.03700 \[astro-ph.CO\]](#).
- [30] T. D. P. Edwards, B. J. Kavanagh, L. Visinelli, and C. Weniger, *Phys. Rev. Lett.* **127**, 131103 (2021), [arXiv:2011.05378 \[hep-ph\]](#).
- [31] J. H. Buckley, P. S. B. Dev, F. Ferrer, and F. P. Huang, *Phys. Rev. D* **103**, 043015 (2021), [arXiv:2004.06486 \[astro-ph.HE\]](#).
- [32] S. Nurmi, E. D. Schiappacasse, and T. T. Yanagida, (2021), [arXiv:2102.05680 \[hep-ph\]](#).
- [33] Y. Bai, X. Du, and Y. Hamada, *JCAP* **01**, 041 (2022), [arXiv:2109.01222 \[astro-ph.CO\]](#).
- [34] A. Prabhu, *Astrophys. J. Lett.* **946**, L52 (2023), [arXiv:2302.11645 \[astro-ph.HE\]](#).
- [35] A. Caputo, A. Philippov, and S. J. Witte, In Prep..
- [36] P. Goldreich and W. H. Julian, *ApJ* **157**, 869 (1969).
- [37] M. A. Ruderman and P. G. Sutherland, *ApJ* **196**, 51 (1975).
- [38] A. Philippov, A. Timokhin, and A. Spitkovsky, *Phys. Rev. Lett.* **124**, 245101 (2020), [arXiv:2001.02236 \[astro-ph.HE\]](#).
- [39] F. Cruz, T. Grismayer, A. Y. Chen, A. Spitkovsky, and L. O. Silva, *ApJL* **919**, L4 (2021), [arXiv:2108.11702 \[astro-ph.HE\]](#).
- [40] K. V. Tilburg, *Physical Review D* **104** (2021), [10.1103/physrevd.104.023019](#).
- [41] R. Lasenby and K. V. Tilburg, *Physical Review D* **104** (2021), [10.1103/physrevd.104.023020](#).
- [42] S. Popov, J. Pons, J. Miralles, P. Boldin, and B. Posselt, *Monthly Notices of the Royal Astronomical Society* **401**, 2675 (2010).
- [43] M. Gullón, J. A. Miralles, D. Viganò, and J. A. Pons, *Monthly Notices of the Royal Astronomical Society* **443**, 1891 (2014).
- [44] A. Spitkovsky, *The Astrophysical Journal* **648**, L51 (2006).
- [45] A. Philippov, A. Tchekhovskoy, and J. G. Li, *Monthly Notices of the Royal Astronomical Society* **441**, 1879 (2014).
- [46] A. Bransgrove, Y. Levin, and A. Beloborodov, *Monthly Notices of the Royal Astronomical Society* **473**, 2771 (2017).
- [47] A. P. Igoshev, S. B. Popov, and R. Hollerbach, *Universe* **7**, 351 (2021).
- [48] D. Viganò, A. Garcia-Garcia, J. A. Pons, C. Dehman, and V. Graber, *Computer Physics Communications* **265**, 108001 (2021), [arXiv:2104.08001 \[astro-ph.HE\]](#).
- [49] D. Viganò, N. Rea, J. A. Pons, R. Perna, D. N. Aguilera, and J. A. Miralles, *Mon. Not. Roy. Astron. Soc.* **434**, 123 (2013), [arXiv:1306.2156 \[astro-ph.SR\]](#).
- [50] S. Johnston and A. Karastergiou, *MNRAS* **467**, 3493 (2017).
- [51] N. Iwamoto, *Phys. Rev. Lett.* **53**, 1198 (1984).
- [52] R. P. Brinkmann and M. S. Turner, *Phys. Rev. D* **38**, 2338 (1988).

- [53] M. Buschmann, C. Dessert, J. W. Foster, A. J. Long, and B. R. Safdi, *Phys. Rev. Lett.* **128**, 091102 (2022).
- [54] G. G. Raffelt, *Stars as laboratories for fundamental physics: The astrophysics of neutrinos, axions, and other weakly interacting particles* (University of Chicago press, 1996).
- [55] N. Iwamoto, *Phys. Rev. D* **64**, 043002 (2001).
- [56] S. P. Harris, J.-F. Fortin, K. Sinha, and M. G. Alford, *Journal of Cosmology and Astroparticle Physics* **2020**, 023 (2020).
- [57] A. Arvanitaki and S. Dubovsky, *Phys. Rev. D* **83**, 044026 (2011), arXiv:1004.3558 [hep-th].
- [58] L. Di Luzio, M. Giannotti, E. Nardi, and L. Visinelli, (2020), arXiv:2003.01100 [hep-ph].
- [59] I. G. Irastorza and J. Redondo, *Prog. Part. Nucl. Phys.* **102**, 89 (2018), arXiv:1801.08127 [hep-ph].
- [60] J. M. Cordes and M. A. McLaughlin, *The Astrophysical Journal* **596**, 1142 (2003).
- [61] A. Caputo, M. Regis, M. Taoso, and S. J. Witte, *JCAP* **03**, 027 (2019), arXiv:1811.08436 [hep-ph].
- [62] P. Sikivie, *Phys. Rev. Lett.* **51**, 1415 (1983).
- [63] S. DePanfilis *et al.*, *Phys. Rev. Lett.* **59**, 839 (1987).
- [64] C. Hagmann, P. Sikivie, N. S. Sullivan, and D. B. Tanner, *Phys. Rev. D* **42**, 1297 (1990).
- [65] C. Hagmann *et al.* (ADMX), *Phys. Rev. Lett.* **80**, 2043 (1998), arXiv:astro-ph/9801286.
- [66] S. J. Asztalos *et al.* (ADMX), *Phys. Rev. D* **64**, 092003 (2001).
- [67] S. J. Asztalos *et al.* (ADMX), *Phys. Rev. Lett.* **104**, 041301 (2010), arXiv:0910.5914 [astro-ph.CO].
- [68] N. Du *et al.* (ADMX), *Phys. Rev. Lett.* **120**, 151301 (2018), arXiv:1804.05750 [hep-ex].
- [69] T. Braine *et al.* (ADMX), *Physical Review Letters* **124** (2020), 10.1103/physrevlett.124.101303.
- [70] R. Bradley *et al.*, *Rev. Mod. Phys.* **75**, 777 (2003).
- [71] S. J. Asztalos *et al.*, *Phys. Rev. D* **69**, 011101 (2004).
- [72] T. M. Shokair *et al.*, *International Journal of Modern Physics A* **29**, 1443004 (2014).
- [73] B. M. Brubaker *et al.* (HAYSTAC), *Phys. Rev. Lett.* **118**, 061302 (2017).
- [74] L. Zhong *et al.* (HAYSTAC), *Physical Review D* **97** (2018), 10.1103/physrevd.97.092001.
- [75] K. M. Backes *et al.* (HAYSTAC), *Nature* **590**, 238 (2021).
- [76] B. T. McAllister *et al.*, “The organ experiment: An axion haloscope above 15 ghz,” (2017), arXiv:1706.00209 [physics.ins-det].
- [77] N. Crescini *et al.* (QUAX), *Phys. Rev. Lett.* **124**, 171801 (2020), arXiv:2001.08940 [hep-ex].
- [78] J. Choi, S. Ahn, B. Ko, S. Lee, and Y. Semertzidis, *NIM-A* **1013**, 165667 (2021).
- [79] A. Álvarez-Melcón *et al.*, *JHEP* **2021** (2021), 10.1007/jhep10(2021)075.
- [80] V. Anastassopoulos *et al.* (CAST), *Nature Physics* **13**, 584–590 (2017).
- [81] D. Wouters and P. Brun, *Astrophys. J.* **772**, 44 (2013), arXiv:1304.0989 [astro-ph.HE].
- [82] A. Abramowski *et al.* (H.E.S.S.), *Phys. Rev. D* **88**, 102003 (2013), arXiv:1311.3148 [astro-ph.HE].
- [83] A. Payez *et al.*, *Journal of Cosmology and Astroparticle Physics* **2015**, 006 (2015).
- [84] M. Ajello *et al.* (Fermi-LAT), *Phys. Rev. Lett.* **116**, 161101 (2016), arXiv:1603.06978 [astro-ph.HE].
- [85] M. Meyer, M. Giannotti, A. Mirizzi, J. Conrad, and M. A. Sánchez-Conde, *Phys. Rev. Lett.* **118**, 011103 (2017), arXiv:1609.02350 [astro-ph.HE].
- [86] M. C. D. Marsh, H. R. Russell, A. C. Fabian, B. P. McNamara, P. Nulsen, and C. S. Reynolds, *JCAP* **12**, 036 (2017), arXiv:1703.07354 [hep-ph].
- [87] C. S. Reynolds, M. C. D. Marsh, H. R. Russell, A. C. Fabian, R. Smith, F. Tombesi, and S. Veilleux, *Astrophys. J.* **890**, 59 (2020), arXiv:1907.05475 [hep-ph].
- [88] M. Xiao, K. M. Perez, M. Giannotti, O. Straniero, A. Mirizzi, B. W. Grefenstette, B. M. Roach, and M. Nynka, *Phys. Rev. Lett.* **126**, 031101 (2021), arXiv:2009.09059 [astro-ph.HE].
- [89] H.-J. Li, J.-G. Guo, X.-J. Bi, S.-J. Lin, and P.-F. Yin, *Phys. Rev. D* **103**, 083003 (2021), arXiv:2008.09464 [astro-ph.HE].
- [90] C. Dessert, J. W. Foster, and B. R. Safdi, *Phys. Rev. Lett.* **125**, 261102 (2020), arXiv:2008.03305 [hep-ph].
- [91] C. Dessert, A. J. Long, and B. R. Safdi, *Physical Review Letters* **128** (2022), 10.1103/physrevlett.128.071102.
- [92] C. Dessert, D. Dunsky, and B. R. Safdi, *Physical Review D* **105** (2022), 10.1103/physrevd.105.103034.
- [93] D. J. Fixsen, A. Kogut, S. Levin, M. Limon, P. Lubin, P. Mirel, M. Seiffert, J. Singal, E. Wollack, T. Villela, and C. A. Wuensche, *ApJ* **734**, 5 (2011).
- [94] M. P. van Haarlem *et al.*, *A&A* **556**, A2 (2013).
- [95] A. T. Sutinjo, D. C. X. Ung, M. Sokolowski, M. Kovaleva, and S. McSweeney, *Astronomy & Astrophysics* **660**, A134 (2022).
- [96] “Proposer’s Guide for the Green Bank Telescope,” <https://www.gb.nrao.edu/scienceDocs/GBTpg.pdf>, accessed: 2023-06-28.
- [97] A. Philippov and M. Kramer, *Annual Review of Astronomy and Astrophysics* **60**, 495 (2022).
- [98] P. Madau and M. Dickinson, *Annual Review of Astronomy and Astrophysics* **52**, 415 (2014).